Università degli Studi di Napoli Federico II

Scuola Politecnica e delle Scienze di Base

Collegio di Scienze

Dipartimento di Fisica "Ettore Pancini"

Corso di Laurea Magistrale in Fisica

TESI DI LAUREA SPERIMENTALE IN FISICA MEDICA

Propagation based phase contrast imaging with a microfocus x-ray tube for breast cancer diagnosis

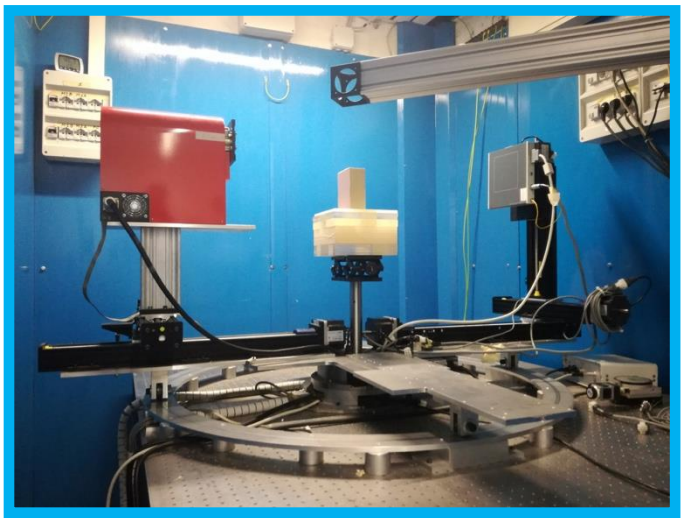

Relatore
Prof. Paolo Russo
Prof. Giovanni Mettivier

Candidata
Dott. Francesca di Franco
Matr. N94/414

Anno Accademico 2017/2018

List of contents

Introduction

Breast cancer is the second leading cause of cancer death in women after lung cancer. Approximately 1 in 8 women in Italy will develop invasive breast cancer during their lifetime. It is the leading cause of cancer mortality in women, with a mortality rate of 17% of all deaths due to cancer [1].

Early diagnosis is a crucial factor in reducing breast cancer mortality. The diagnostic method should have high specificity and sensitivity, should be non-invasive and harmless.

Today breast cancer diagnosis is made by three steps: physical examination, breast imaging and biopsy.

Mammography, where the radiographic contrast is due to absorption of X-rays, is the most wildly used and the only breast imaging method for mortality reduction. The sensitivity of mammography for the detection of breast cancer in non-dense breasts has been reported to be 85% [2]. On the other hand, the sensitivity drops to 48% in women with extremely dense breasts (greater than 75% fibro-glandular tissue), because tumor and dense breast tissue both appear with the same shade of gray on a mammogram [3].

In the last years the attention has been focused on a new X-ray imaging technique, Phase-Contrast X-ray Imaging (PCI), which use information of the changes in the phase of an X-ray beam that passes through an object, in order to provide a better image contrast.

Conventional X-ray imaging uses the drop in intensity by attenuation caused by an object in the X-ray beam and the radiation is treated as rays like in geometrical optics. However, when X-rays pass through an object, not only their amplitude but their phase is altered as well, since X-rays can also be treated as electromagnetic waves.

X-ray phase-contrast mammography (PCM) and X-ray phase-contrast Computed Tomography are a recent X-ray imaging based on an image contrast mechanism different from the X-ray absorption technique. For soft tissue, at clinical energies, the image contrast due to phase-contrast maybe higher than absorption contrast.

Several methods for X-ray phase-contrast imaging have been developed in the last years and they can be divided in three main classes: interferometric methods using crystals, analyzer based and propagation-based methods. These three methods differ for the experimental setup and for the radiation source used.

In particular, our attention will be focalized on propagation-based phase-contrast imaging technique that involves the simplest configuration because it does not involve the introduction of any optical element between the sample and detector.

A micro focus source generates a partially coherent x-ray beam which traverses a sample, and a sample-to detector distance is introduced to create an interference patterns on the imaging plane. Contrast is generated from the interference among parts of the wave fronts that have experienced different phase shifts. Such contrast is superimposed to the absorption image and might help to improve the visibility of the borders of structures and other details.

In this study, we compared the detectability of a test pattern embedded in a breast phantom using high energy in-line phase sensitive technique. The aim of this work was to investigate the possible improvement in contrast in phase-contrast imaging with respect to attenuation-based imaging. In particular, we investigated the image quality for detection of simulated micro-calcifications and masses in a breast mammographic phantom (50% glandular/50% adipose).

The images are acquired in absorption-based and propagation-based phase-contrast 2D imaging, propagation-based phase-contrast CT, propagation-based phase-contrast tomosynthesis and at least we use a phase retrieval algorithm to obtain the phase map of the phantom.

This thesis is divided in two chapters. The first chapter illustrates the physical principle of phase-contrast X-ray imaging and the second chapter contains the experimental results of this thesis and their discussion.

Chapter 1: Phase Contrast Imaging

The german physicist Wilhelm Röntgen discovered X-rays in 1895, because he was the first to systematically study them, though he is not the first to have observed their effects.
X-rays shared with visible light the ability to imprint photographic plates and Röntgen wanted to look for other effect as diffraction and refraction, so Rontgen was looking for phase effect in the X-ray beam but he could not find any evidence of reflection and refraction.
The study of the electromagnetic nature of X-rays started with the work of two Dutch physicists Haga and Wind who observed for the first time the X-ray diffraction from a slit (1899). After them, the two Bragg observed the X-ray diffraction from crystals (1913).
Today many experimental techniques are based on the wave nature of the X-ray fields and the classical diffraction theory can be applied to X-ray waves as for the light waves, so X-ray phase effects in imaging can be used alongside attenuation effects [4].

1.1 Theory of X-ray phase contrast

Let us consider the scalar field function $\psi\,(x, y, z, t)$ that is the solution of the d'Alembert equation in vacuum:

$$\left(\frac{1}{c^2}\,\frac{\partial^2}{\partial t^2} - \,\nabla^2\right)\,\psi(x, y, z, t) = \,0 \tag{1}$$

Using the Fourier integral, we can decompose $\psi\,(x, y, z, t)$ into monochromatic components:

$$\psi(x, y, z, t) = \,\frac{1}{\sqrt{2\pi}}\int_0^\infty \psi_\omega(x, y, z)e^{-i\omega t} \tag{2}$$

Each monochromatic component is the product of a spatial part ($\psi_\omega(x, y, z)$) and an harmonic time-dependent term ($e^{-i\omega t}$). Substituting (2) in (1), it is simple to verify that the spatial part of each monochromatic term must satisfy the Helmholtz equation:

$$(\nabla^2 + k^2)\psi_\omega(x, y, z) = 0 \tag{3}$$

This is the key equation underpinning most of the results in X-ray phase contrast imaging. Helmholtz equation is useful in describing an imaging process when the X-ray beam is monochromatic but most of the radiological imaging is done with polychromatic X-rays generated by X-ray tubes.

Spectral decomposition of the wave function into monochromatic components enables the description of imaging process with a time-independent approach which can then combined to obtain the complete description of the polychromatic process.

If we consider an electromagnetic beam, the energy is concentrated within a small region in proximity of the beam axis with small spread. An electromagnetic field with these proprieties is called paraxial field, such as a laser beam.

In most situations involving phase contrast imaging, X-ray fields behave as a paraxial field, so it is possible to apply the mathematical formalism of paraxial fields to phase contrast imaging. This is a great advantage because simplifies the equations involved and enables a simple algorithm for phase retrieval.

If we consider the solution of the Helmholtz equations $\psi_\omega(x, y, z)$, we can describe a field as a paraxial field when:

$$\psi_\omega(x, y, z) = \phi\,(x, y, z)e^{-ikz} \tag{4}$$

The variation of the longitudinal position (z) of the complex envelope $\phi\,(x, y, z)$ is smaller than its variations in the transverse plane (x, y). In this way $\psi_\omega(x, y, z)$ displays beam-like propagation properties along z-axis, so its complex envelope $\phi\,(x, y, z)$, which is slowly variating, is modulated by a carrier plane wave e^{-ikz}.

Formally, the condition of nearly longitudinal propagation can be described noting that the variation $\Delta\phi\,(x, y, z)$ within a longitudinal distance $\Delta z = \lambda = 2\pi/k$, have to be smaller than $\phi\,(x, y, z)$:

$$\frac{\Delta\phi\,(x, y, z)}{\phi\,(x, y, z)} \ll 1 \tag{5}$$

Since $\Delta\phi\,(x, y, z) = (\partial\phi\,(x, y, z)\,/\partial z)\Delta z = (\partial\phi(x, y, z)/\,\partial z)\,\lambda$:

$$\frac{\partial\phi\,(x, y, z)}{\partial z} \ll k\phi\,(x, y, z) \tag{6}$$

The same condition for the second derivative is:

$$\frac{\partial^2\phi\,(x, y, z)}{\partial z^2} \ll k^2\phi\,(x, y, z) \tag{7}$$

The equation (7) can be used as a formal definition of a paraxial field.

Substituting (4) in (3) we can obtain the paraxial Helmholtz equation:

$$\nabla_T^2 \phi\,(x,y,z) + 2ik\frac{\partial \phi\,(x,y,z)}{\partial z} = 0 \tag{8}$$

Where ∇_T^2 is the transverse Laplacian and (8) is the approximation of Helmholtz equation under the condition of slowly varying envelope.

All equations we derived are valid in vacuum but any phase contrast imaging effect needs the interaction of the radiation with a sample, so all the equations must be generalized in presence of media introducing the refractive index $n(x,y,z)$ defined as:

$$n(\mathrm{x},\mathrm{y},\mathrm{z}) = \left(\frac{\varepsilon(x,y,z)}{\varepsilon_0}\right)^{1/2} \tag{9}$$

Where $\varepsilon(x,y,z)$ is the electrical permittivity of the material and ε_0 is the electrical permittivity in vacuum.

The d'Alembert and the other equations are valid for a scalar field but it is an approximation because the wave function is a vectorial quantity describing the evolution of both electric and magnetic fields, so a single scalar equation is not sufficient when polarization effects occurs.

In hard X-ray imaging the variations in the optical density of any media are slowly varying over length scales comparable to the wavelength so electric and magnetic field components can be considered decoupled. This justifies the approximation of using a scalar theory to study X-ray wave propagation.

Following the same procedure, we discussed in vacuum, each monochromatic component obeys the inhomogeneous Helmholtz equation:

$$(\nabla^2 + n^2(x,y,z)k^2)\,\psi(x,y,z) = 0 \tag{10}$$

It is also possible to consider valid the paraxiality conditions and we can write the inhomogeneous Helmholtz equation:

$$\nabla_T^2 \phi\,(x,y,z) + 2ik\frac{\partial \phi\,(x,y,z)}{\partial z} + k^2(n^2(x,y,z)-1)\phi\,(x,y,z) = 0 \tag{11}$$

Using (11) it is possible to study X-ray phase contrast effects in imaging [4].

1.1.1 Complex refractive index

It is well known that the refractive index of optical materials for visible light is larger than 1 and 1 is the refractive index of vacuum. The refractive index has particular characteristics in the X-ray region, the difference from unity is extremely small (10^{-6} for hard X-ray) and the attenuation effects are non-negligible. The X-ray complex refractive index is:

$$n = 1 - \delta + i\beta \tag{12}$$

The real δ part is related to the refraction and the imaginary part β, to the absorption.

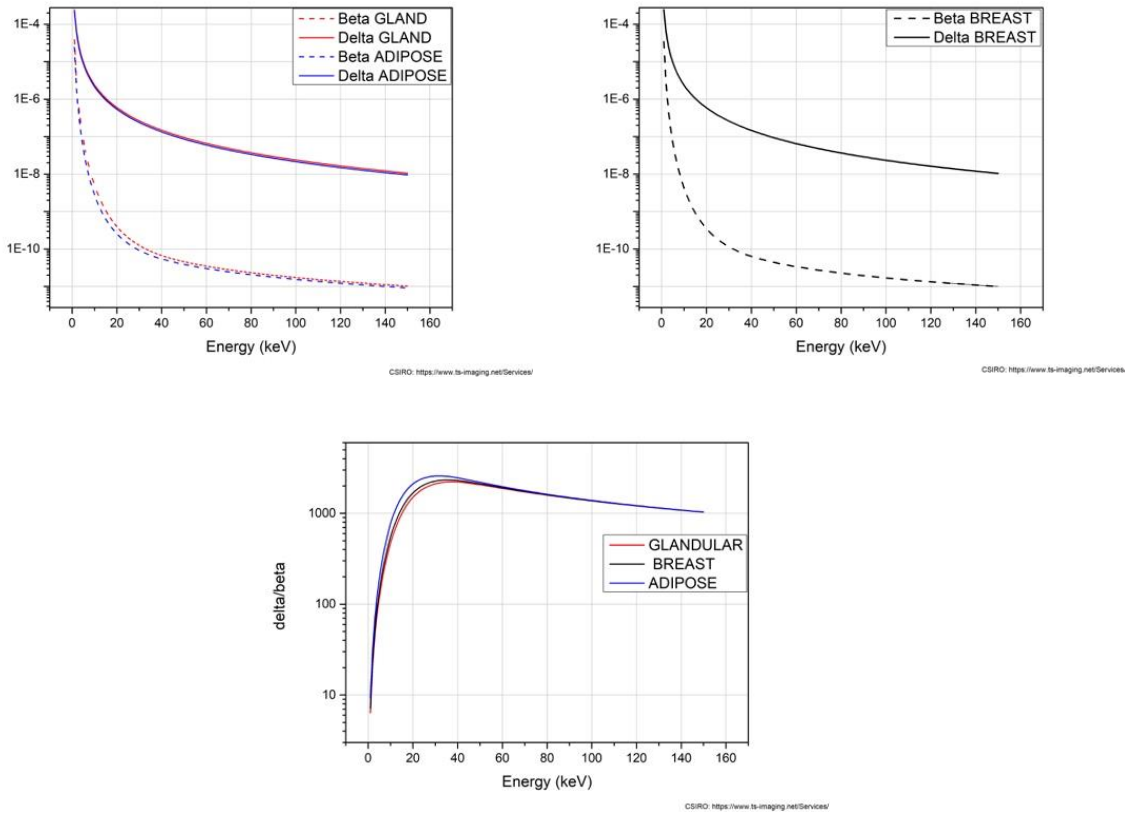

Figure 1: (a), (b) calculated values of the refractive index for three representative tissues: adipose, glandular and breast tissue. In all cases the real part, δ, the refractive index is plotted with solid lines and the imaginary part, β, is plotted with dashed lines. (c) δ/β ratio for three representative tissues.

Figure 1 shows the calculated values of δ and β for three representative tissues. It is easy to see that the real part of the refractive index is always about two order of magnitude larger than the imaginary part.

The absorption imaging is related to the imaginary part of the refractive index, instead the phase contrast imaging is related to the real part. In the spectral region of interest for radiology, it is always $\delta \gg \beta$, so a phase contrast is stronger than attenuation contrast. Phase contras may offer an advantage when one needs to distinguish between different types of soft tissues.
The complex refractive index is small, so most of the X-rays that are passing through an object do not interact with the object and the resulting image contrast is poorer than in other imaging techniques.

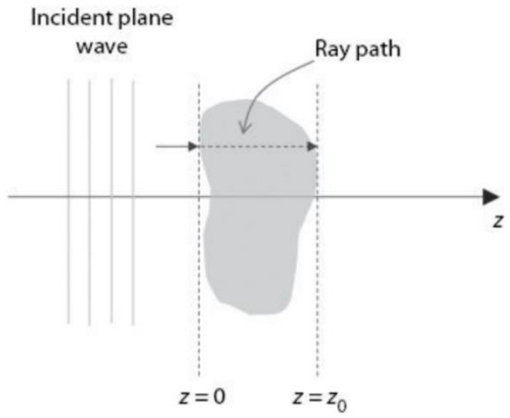

Figure 2: Schematic diagram showing the ideal path that the X-rays would cover in geometric approximation in absence of the sample. The projection approximation is equivalent to discarding any change in the ray path introduced by the presence of the sample [4].

The projection approximation is an extremely useful approximation of the interaction of X-rays with matter. With reference to figure 2 we consider a plane wave incident on a sample along the positive z-direction. At any position along the sample, we can consider the "ray path" as the trajectory defined by the wave vector in absence of the sample (dashed arrow). We assume that the scattering that takes place within the sample is negligible, so all scattering within the sample can be described by an exit wave defined at a plane $z = z_0$, doing this is equivalent to remove the Laplacian term in (11):

$$2ik\frac{\partial\phi(x,y,z)}{\partial z} + k^2(n^2(x,y,z) - 1)\phi(x,y,z) = 0 \qquad (13)$$

This approximation describes the passage of rays through an object, defining a nominal exit surface downstream the irradiated object and assumes that all scattering within the object is described by the exit wave.
The boundary problem for the equation (13) can be solved yielding the wave field at the position $z = z_0$:

$$\phi\,(x,y,z_0) = exp\left[\frac{k}{2i}\int_0^{z_0}\left(1-n^2(x,y,z)\right)dz\right]\phi\,(x,y,0) \tag{14}$$

The complex refractive index is usually written as in (12) where δ, $\beta \ll 1$ are related to the microscopic scattering coefficients of the interaction of X-ray with matter. At this point, we can say that $n^2 \approx 1 - 2\delta + 2i\beta$:

$$\phi\,(x,y,z_0) = exp\left[-ik\int_0^{z_0}\left(\delta(x,y,z) - i\beta(x,y,z)\right)dz\right]\phi\,(x,y,0) \tag{15}$$

This formula gives us an expression for the phase shift and attenuation that an X-ray wave undergoes when crossing a sample, in the projection approximation.

The phase shift is given by the imaginary part of the exponent $\Delta\phi = -k\int_0^{z_0}\delta(x,y,z)dz$ and the attenuation by its real part, $-k\int_0^{z_0}\beta(x,y,z)dz$. If we consider a single homogeneous material, δ and β are independent of the position and the transmitted wave field can be written as:

$$\phi\,(x,y,z_0) = exp[-k(i\delta+\beta)t(x,y)]\phi\,(x,y,0) \tag{16}$$

where $t(x,y)$ is the projected thickness of the sample along the ray path.

The intensity transmitted after the sample is:

$$I(x,y,z_0) = \exp[-\mu t(x,y)]\,I(x,y,0) \tag{17}$$

(17) is the Lambert-Beer law of attenuation, where the attenuation coefficient is:

$$\mu = 2k\beta = 4\pi\beta/\lambda \tag{18}$$

It is important to say that is not possible to measure the phase contrast from a conventional radiograph, because any conventional detector will produce an intensity measurement proportional to the square modulus of the complex wave field and the information about the phase shift produced by the sample is lost but there are other ways to access the phase information.

If we assume that a plane wave has interacted with a sample and the complex wave field after the sample is $\phi\ (x, y, z_0)$ which is propagating in the vacuum. In this way at any position $z > z_0$ the field can be described by the paraxial homogeneous Helmholtz equation.
We can rewrite the complex envelope as:

$$\phi\ (x, y, z_0) = \sqrt{I(x, y, z_0)}\ e^{i\varphi(x,y,z_0)} \tag{19}$$

Substituting (18) into the paraxial homogeneous Helmholtz equation (where the imaginary part is equal to zero), we obtain the Transport of Intensity equation (TIE):

$$\nabla_T[I(x, y, z_0)\ \nabla_T\varphi(x, y, z_0)] + k\ \frac{\partial I(x, y, z_0)}{\partial z} = 0 \tag{20}$$

The TIE equation provides a relationship between the intensity of a slowly varying envelope and the corresponding phase, in the paraxial approximation.
From the Lambert-Beer's equation is clear that the phase shift imparted by the sample cannot be extracted by conventional radiography but all the process which gave us the TIE equation suggest that the intensity measured after the beam propagates further downstream in free space contains phase information. This information cannot be recovered during imaging process, so there are some algorithms useful to retrieve the phase information from the images [4].

1.2 Phase contrast X-ray imaging techniques

The development of X-ray phase-contrast imaging (XPCI) is possibly related to the relatively weak interaction of X-rays with matter: in the complex refraction index (12), both the refractive index decrement (δ) and the imaginary part (β) are very small. As a consequence, the deviations suffered by X-ray photons are too small to be detected (microradians scale), unless specific phase sensitive techniques are used. Most of these techniques require intense and highly coherent X-rays, for this reason XPCI has increasingly expanded in the last two decades, together with new synchrotron radiation sources.
Several XPCI techniques have been introduced including: crystal X-ray interferometry, analyzer based phase contrast imaging, propagation based phase contrast imaging (PBI), edge illumination (EI) and X-ray interferometry. Three of them (PBI, ABI and EI) are non-interferometric methods which are used in medical imaging [5].

1.2.1 Propagation based phase contrast imaging (PBI)

PBI is the simplest method, because no X-ray optical devices are needed. The source must be small to provide transverse (spatial) coherence of the beam.

The phase changes are smooth and the Laplacian small, except at the lateral edges, where the transverse phase profile changes sharply.

Sufficient distance between the sample and the detector is required, typically a few meters. There are also several methods for phase retrieval from the observer intensity distribution. These involve various approximations, which are needed to separate the contributions of absorption and phase.

PBI is probably the method that will have the widest clinical applications when the phase retrieval algorithms will be routinely used, due to its experimental simplicity.

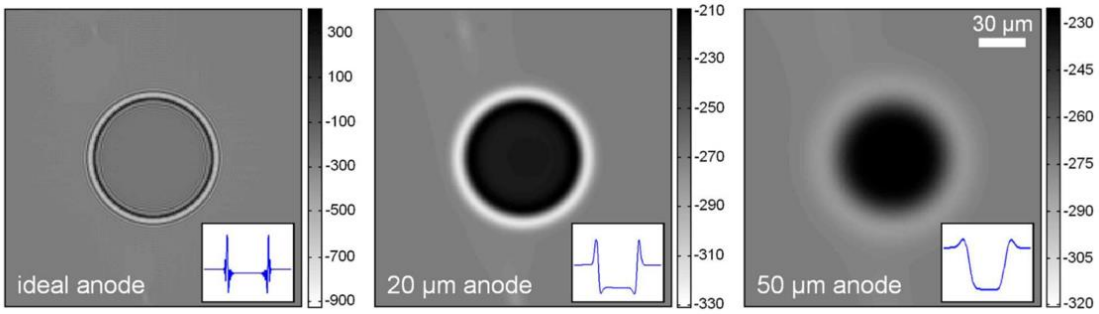

Figure 3: Simulated images of a spherical micro-calcification in PBI with a Konica Minolta system. Blurring of the intensity due to the source size is shown in the inserts. [6]

It is important to underline two of the most important request of the PBI method: the first is the distance between the detector and the object. It is easy to understand that there is a huge difference between the conventional absorption-based imaging technique, where the detector is immediately behind the object

The other request is the presence of a X-ray beam with a high degree of coherence, so the detector must have sufficient special resolution to capture the fringes arising upon propagation.

The object to detector distance, z_{od}, should be compared to a^2/λ, where λ is the X-ray wavelength and a is the size of the smallest detail of interest in the sample.

When $z_{od} \ll {a^2}/{\lambda}$ (near-field region) a characteristic profile is recorded with one positive and one negative peak in correspondence with the detail edges. If $z_{od} \cong {a^2}/{\lambda}$ (intermediate region: Fresnel diffraction) the object image is slightly distorted, presenting an interference pattern with several oscillations in correspondence of each edges.

In the end, if $z_{od} \gg {a^2}/{\lambda}$ (far-field region: Fraunhofer diffraction) the intensity pattern at the detector plane has little resemblance to the object but can still be used for imaging in case of small samples and highly coherent beams. In medical X-ray imaging, typical values for $a \; and \; \lambda$ are 10^{-5} m and 10^{-10} m respectively, which makes ${a^2}/{\lambda}$ of the order of 1 meter.

We know that the most interesting applications in medical imaging have been obtained in the near-field region. The edge enhancement images obtained in this case can be used without further processing, since the improved visualization of the detail is often sufficient to highlight its presence, even in case of low absorption contrast. Alternatively, a phase retrieval procedure can be utilized. This procedure has two advantage: the first one it is possible to obtain quantitative parametric images, especially when the sample is in particular conditions (weak absorption or a ${\delta}/{\beta}$ nearly constant) and the second advantage is that phase retrieval can improve the visualization of the detail (especially in noisy images) since the edge enhancement makes the image interpretation easier [5].

1.3 Screening and diagnostic Mammography

Brest cancer is one of the major cause of female mortality in industrialized countries. Early diagnosis is a crucial factor in reducing breast cancer mortality. The diagnostic method should have high specificity and sensitivity, be non invasive and harmless as possible.

Breast cancer diagnosis is made by three steps: physical examination, breast imaging and fine-needle aspiration or biopsy.

Mammography, where the radiographic contrast is due to absorption of X-rays, is the most used and the only evidence based breast imaging method for mortality reduction. The specificity of X-ray absorption contrast mammography is strongly affected by breast density. For breast cancer survival, the time of diagnosis is extremely important since tumor size and stage ad diagnosis are the most important prognostic indicators. Different incidence, mortality and survival rates are due to differing risk factors, availability of screening programs and access to effective treatment.

Diagnostic X-ray imaging is an additional examination used for differentiation of malignancies from benign breast diseases as well as their localization, classification and extent evaluation.

The most common signs of abnormalities encountered in mammograms are masses and calcifications whose radiographic appearances provide important clues to their etiology.

In X-ray absorption contrast mammography almost all cancers will be apparent in fatty breasts. Radiolucent adipose tissue provides an excellent background for detecting even small abnormalities. Mammography can also provide excellent visibility of calcifications, which are present in 45% to 65% of breast malignancies and in about 20% of benign diseases.

The major challenge of mammography is the detection of cancer, particularly in pre-menopausal women with predominantly dense breasts: only half tumors are visible in extremely dense breast because the sensitivity is inversely proportional to the breast density and it declines down to 30% in women with extremely dense breast.

Ideally the breast should be imaged in three dimensions with good contrast and high spatial resolution, while keeping the radiation dose to an acceptable level. To reach this type of imaging in these years have been developed many imaging techniques dedicated to the breast. Dedicated breast computed tomography (CT) was introduced almost 20 years ago and important advances have been seen in digital breast tomosynthesis (DBT) which is a 3D imaging technique where low dose images are acquired and reconstructed into thin slices, reducing the effect of overlapping tissue and facilitating breast cancer detection.

It is quite sure that DBT will be a strong alternative to planar mammography, both for screening and diagnosis because studies have shown a significant increase of breast cancer detection (30%-40%) [5].

1.4 X-ray phase contrast Mammography

X-ray phase contrast mammography (PCM) is a quite recent X-ray imaging technique developed to overcome the insufficient image contrast of the X-ray absorption mammography. The first limitation to obtain high contrast images in the clinic is the limitation on the dose delivered to the patient so this requires that the X-ray energy should be high enough to limit the absorbed dose but means low contrast. For soft tissue, at clinical energies, the image contrast due to phase contrast is significantly higher than absorption contrast.
Technical developments have been produced so that phase-contrast imaging could be used in clinical applications. Most experimental results have been obtained by analyzer-based phase contrast imaging (ABI) and propagation-based phase contrast imaging (PBI) has been used in pre-clinical studies.

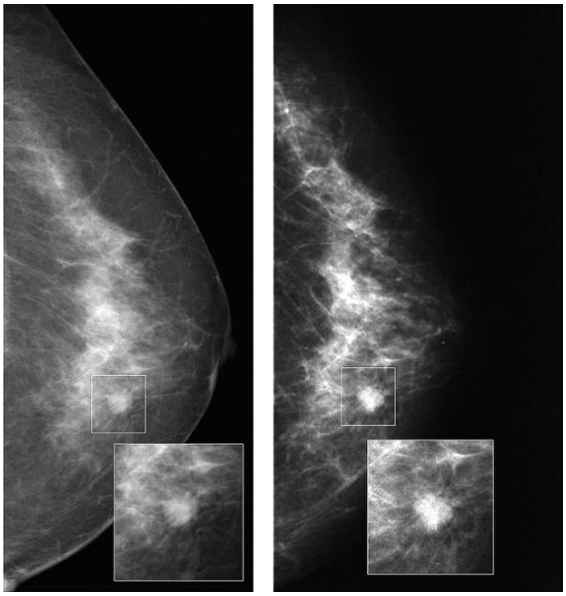

Figure 4: Comparison of mammograms from SYRMEP: left image is a digital mammography and the right image is a PBI mammography [7]

A recent clinical trial of phase-contrast mammography with synchrotron radiation was performed at the SYRMEP beamline of the Elettra synchrotron in Trieste, Italy [9,10]. All 47 patients who completed this trial had previously undergone digital mammography and ultrasound examinations at a local hospital but received an unclear diagnosis. In this patient

population, the reference clinical mammograms had a specificity and sensitivity of 52% and 69%, respectively, whereas PBI mammography at the synchrotron resulted in specificity and sensitivity values of 94% and 81% [9]. In each case, either biopsy or 1-year follow-up was used as the standard of reference. This outcome suggests that PBI mammography with 34isynchrotron radiation may increase the number of true negatives and may therefore be particularly suitable as a second-level examination following clinical mammography.
Improved image quality in this trial (figure 4) can be partially attributed to improved X-ray beam characteristics at the synchrotron, such as monochromaticity, non-divergence and spatial coherence, rather than the phase effect itself [5] [8].

1.5 X-ray phase contrast Computed Tomography

CT studies on isolated tumor-bearing breast tissue samples and recorded with synchrotron radiation yield images with excellent soft-tissue contrast compared with absorption-based images of the same specimens. The improved visibility of tissue morphology and collagen architecture provides evidence that phase contrast imaging can obtain radiological images with excellent correspondence to histology, suggesting that phase-contrast CT may allow deeper insight into the fine structure of tissue than conventional imaging modalities. Phase-contrast CT could assist ex vivo tissue analysis following surgery, when rapid evaluation of tumor boundaries is needed for surgical quality control. Furthermore, it may assist breast cancer diagnosis by providing advanced insight into tumor morphology and differentiation between cancerous and unaffected tissues. Pani et al [11] have evaluated the feasibility of breast tomography at the Elettra synchrotron radiation facility, using in vivo breast imaging set-up. Their analysis of fresh post-mortem whole breast samples from healthy donors shows that phase-contrast breast CT can be recorded at clinically accepted radiation dose. It should be noted, however, that the phase-contrast breast tomography studies mentioned above were carried out at synchrotron X- ray sources, where rotating gantries cannot be implemented. A first study of phase-contrast breast CT using conventional X-ray tubes has been published by Grandl et al [12]. The authors show that grating-based phase- contrast CT at a conventional X-ray source provides complementary information to conventional absorption contrast, albeit at radiation doses far exceeding those deemed clinically acceptable [5] [8].

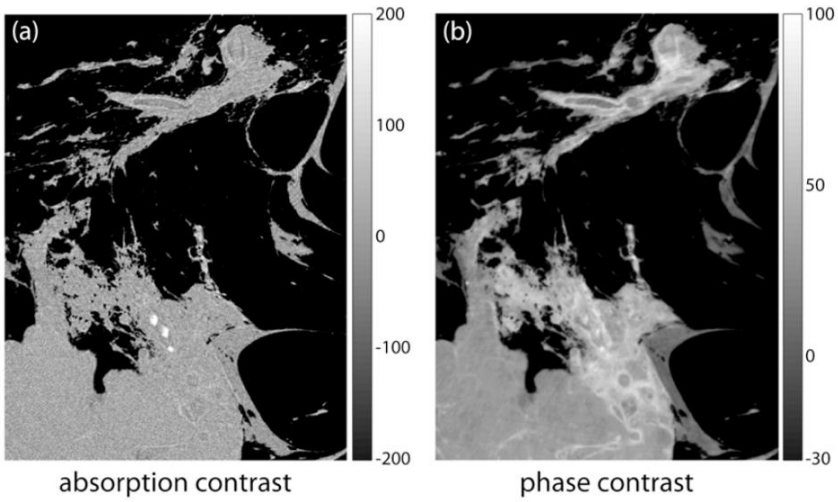

Figure 5: Direct comparison of absorption and phase-contrast breast CT. Experimental absorption-contrast (a) and phase-contrast (b) tomographic images recorded at the European synchrotron radiation facility. The grey-scale bars represent Hounsfield units (absorption contrast) and phase-contrast Hounsfield units (phase contrast), respectively. The sample presented here contains invasive ductal carcinoma, as well as ductal carcinoma in situ. Phase-contrast images reveal contrast differences within the tumor that are not resolved by absorption-based imaging. In particular, circular structures of high phase contrast within ductal carcinoma in situ are better resolved in phase-contrast images and coincide with ductal walls and the basement membrane. Conversely, calcifications are better seen in absorption-based images, underlining the complementary nature of the methods. [8]

1.6 Phase retrieval algorithm

Phase contrast image is an image produced by a phase contrast imaging system, in which phase variations in a given wave-field were transformed into visible intensity variations in the detector plane. Detectors reveal the intensity distribution $I(x;\ y;\ z)$ and we want to retrieve the phase map distribution $\phi(x, y)$.

The problem of retrieve the phase distribution of the input wave-field is recognized as an inverse problem: from measured data to the model. This problem arises because of the rapid oscillation frequencies of the X-ray wave field.

In general phase retrieval problem requires almost two measurement of intensity, taken at two different distance from the source: a contact image which takes into account only the information about absorption and a second image taken away from the sample.

Paganin et al. [13] developed and applied a method for quantitative phase extraction using a single propagation-induced phase contrast image.

To briefly describe this algorithm, we start using the Transport of Intensity equation (20) which describes the intensity evolution of a paraxial monochromatic scalar electromagnetic or matter wave on propagation. In (20) the intensity and the phase of the beam are denoted by $I(x, y, z_0)$ and $\varphi(x, y, z_0)$.

Now we want to find a solution of (20) for the phase $\varphi(x, y, z_0)$, given non-interferometric measurements of $I(x, y, z_0)$ and its derivative.

To simplify the extraction of phase information from a single image, is useful assuming that the point-source of the X-ray is at infinity (in Figure 7, $R_1 \to \infty$) and that the object under study is composed by a single homogeneous material.

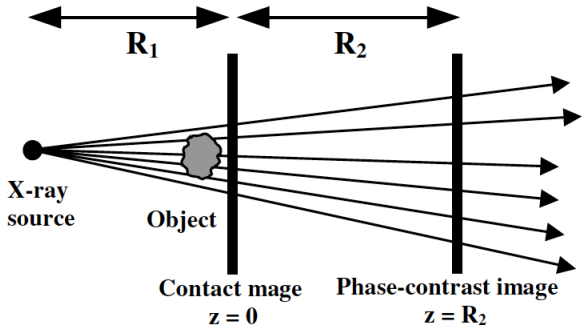

Figure 6: Schematic representation of phase-contrast geometry using a point source [13].

The intensity of the radiation over the plane at exit surface $z = 0$ (contact image) of the object is assumed to be well approximated by Lambert-Beer's law:

$$I(r_\perp, z) = I^{in} e^{-\mu T(r_\perp)} \tag{21}$$

$T(r_\perp)$ is the projected thickness of the homogeneous object onto the plane over which the image is taken, μ is the linear attenuation coefficient, and I^{in} is the uniform intensity of the incident radiation. If the object is sufficiently thin, the phase $\varphi(r_\perp, z = 0)$ of the illuminating beam at the exit surface of the homogeneous object is proportional to the projected thickness:

$$\varphi(r_\perp, z = 0) = -\frac{2\pi}{\lambda} \delta\, T(r_\perp) \tag{22}$$

Representing the contact image and the phase contrast image as Fourier integral, through some mathematical passages:

$$F\left\{e^{-\mu T(r_\perp)}\right\} = \mu \frac{F\{I(r_\perp, z = R_2)/I_0\}}{R_2 \delta |k_\perp|^2 + \mu} \tag{23}$$

Taking the inverse Fourier transform of (22) and solving for $T(r_\perp)$:

$$T(r_\perp) = -\frac{1}{\mu} ln\left(F^{-1}\left\{\mu \frac{F\{I(r_\perp, z = R_2)/I_0\}}{R_2\delta|k_\perp|^2 + \mu}\right\}\right) \tag{24}$$

Removing the assumption of infinitely distant point source and using the Fresnel diffraction integral, it is possible to show that the intensity $I_R(r_\perp, z)$ downstream of a weakly refracting object illuminated by a point source at distance R_1behind the object, is related to the intensity $I_\infty(r_\perp, z)$. We can now transform (23) into an alternative form:

$$T(r_\perp) = -\frac{1}{\mu} \log_e\left(F^{-1}\left\{\mu \frac{F\{M^2 I(Mr_\perp, z = R_2)/I^{in}\}}{R_2\delta|k_\perp|^2/M + \mu}\right\}\right) \tag{25}$$

where $M = (R_1 + R_2)/R_1$ is the image magnification. This result shows how to solve the Transport of Intensity equation (20) for the projected thickness, using a single defocused image. The algorithm is characterized by high stability due to the presence of a non-zero linear attenuation coefficient which avoids mathematical problem of the division by zero [13].

Chapter 2: Measurements and data analysis

The experimental work done for this thesis has been carried out in the laboratory of medical physics of this department, using a micro-focus X-ray tube.

The aim of this work is to investigate the improvement in image quality using phase-contrast imaging with respect to attenuation-based imaging. A phantom study was conducted in order to test the capability of these two imaging techniques in showing phantom micro-calcifications and masses.

In this chapter will be described the experimental setup and the image acquisition method. At the end will be presented all results and their discussion.

2.1 Experimental setup

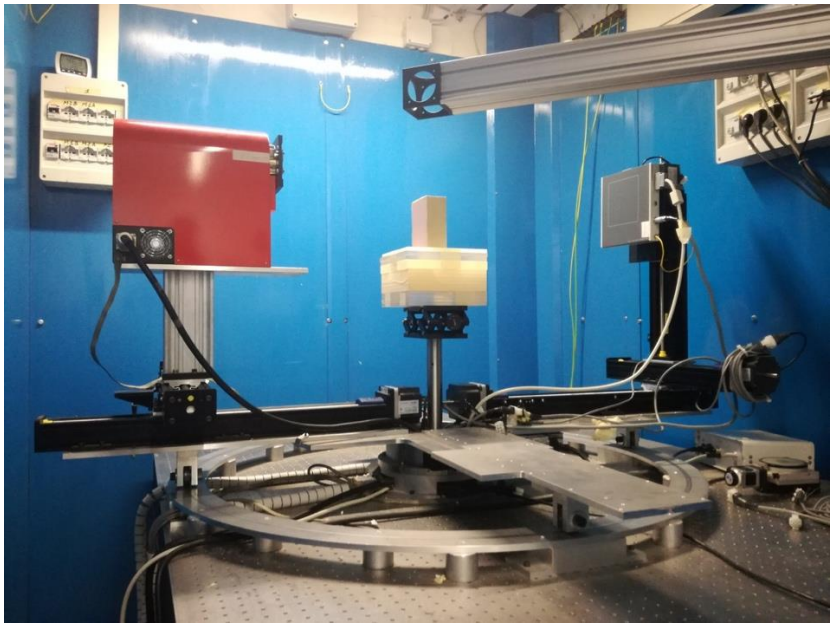

Figure 7: Cone-beam microCT prototype scanner dedicated to breast imaging. Microfocus X-ray tube and CMOS flat panel detector, mounted on a step-motor linear stages for variable-magnification imaging. Step-motor rotating gantry; breast phantom placed at isocenter and simulating a compressed breast; post and lab jack at isocenter for hosting phantoms. Step-motor linear stages and rotation stages are used for setting the acquisition geometry and for gantry rotation.

2.1.1 Flat panel detector

The detector used is a CMOS flat panel detector (Hamamatsu mod. C7942CA-02), an indirect detector with a sensitive area of 12 cm x 12 cm (2400 x 2400 pixels), a 50 μm pixel pitch and containing a 150 μm thick CsI:Tl scintillator layer which converts the x-rays into light. Directly behind the scintillator layer is an amorphous silicon detector array made up of millions of pixels each containing a thin-film transistor forming a grid patterned in amorphous silicon on the glass substrate. Each pixel also contains a photodiode which generates an electrical signal in proportion to the light produced by the portion of scintillator layer in front of the pixel. The signals from the photodiodes are amplified and encoded by additional electronics positioned at the edges or behind the sensor array in order to produce an accurate and sensitive digital representation of the x-ray image.

The signal acquired is sent to an acquisition board which is inserted in a computer. Using the acquisition board is possible to modify some parameters as binning mode or frame rate.

The binning mode will combine the information of adjacent pixels so this lead to a reduced resolution by the factor of binning. However, is possible to acquire images using the maximum spatial resolution of 8 lp/mm.

The frame rate, instead, allows to fix the sampling frequency of signal between 0.1 and 9 fps (frame per second). A software is used in order to control acquisition procedures and to set the scanner geometry. [14]

Figure 8: CMOS flat panel detector (Hamamatsu mod. C7942CA-02).

2.1.2 X-ray tube

The X-ray tube used is a microfocus X-ray tube (Hamamatsu mod. L8121-03, fig. 9) with a selectable focal spot whose size of 7, 20 or 50 μm with a maximum power of 10, 30 and 75 W. This air-cooled tube has a fixed tungsten anode, a cone angle of 43°, the output window is made of 0.2 mm Be of inner filtration and the added filtration is variable, depending on the requirements. The X-ray tube can be operated at a constant voltage between 40 kV and 150 kV [14].

F

igure 9: Microfocus X-ray tube (Hamamatsu mod. L8121-03)

Using the characteristic curve (fig. 10), it is possible to determinate the maximum tube current value when the focal spot size is fixed.

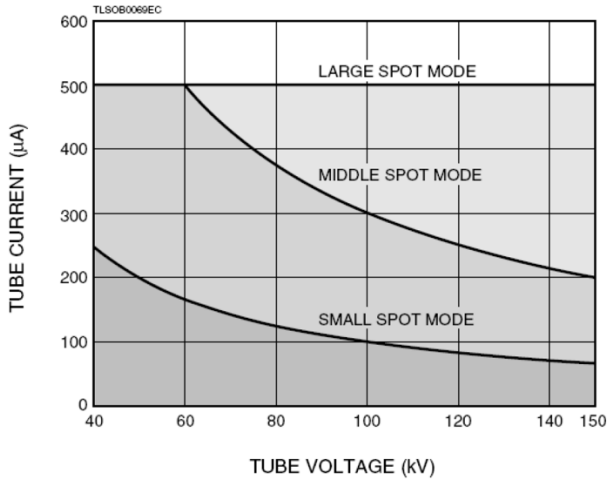

Figure 10: Characteristic current-voltage curves for three different focal spot size.

2.1.2 CIRS phantom

The CIRS (Computerized Imaging Reference System Inc., Norfolk, USA) is one of the leader in the manufacturer of tissue equivalent phantoms and simulations for medical imaging and dosimetry.

The phantom used in this work is CIRS – 014AD, which is used for quality control in mammography. Our phantom is made up of six slabs (table 1, fig 11) simulating homogeneous mammalian tissue (BR 50/50): 50% glandular tissue and 50% fat tissue. The elemental composition of the phantom is based on studies carried out on human tissues [15] [16].

	# Slabs	Width (cm)	Height (cm)	Length (cm)
Br 50/50 014AD	3	2	10	12.5
	2	1	10	12.5
	1	0.5	10	12.5

Table 1: Features of phantom CIRS – 014AD

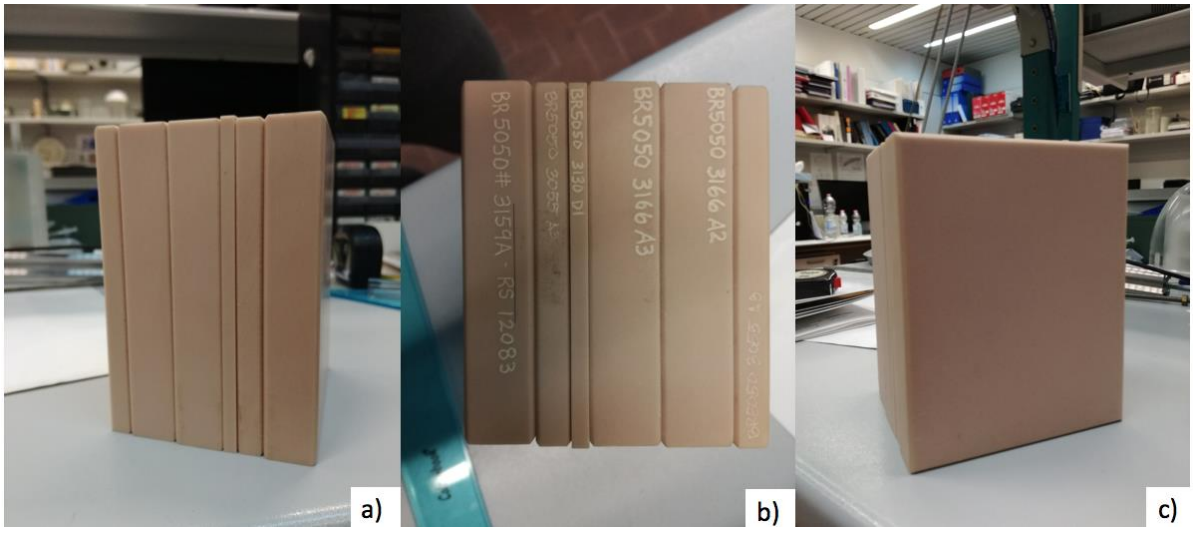

Figure 11: Photographs of the whole phantom CIRS – 014AD: 1) lateral view; 2) top view; 3) frontal view

One of the three slabs of 2 cm thick contains a test pattern made up of microcalcifications, masses and other details specified in figure 12. For our purpose, only three of six slabs have been used, creating a phantom of 5 cm thick.

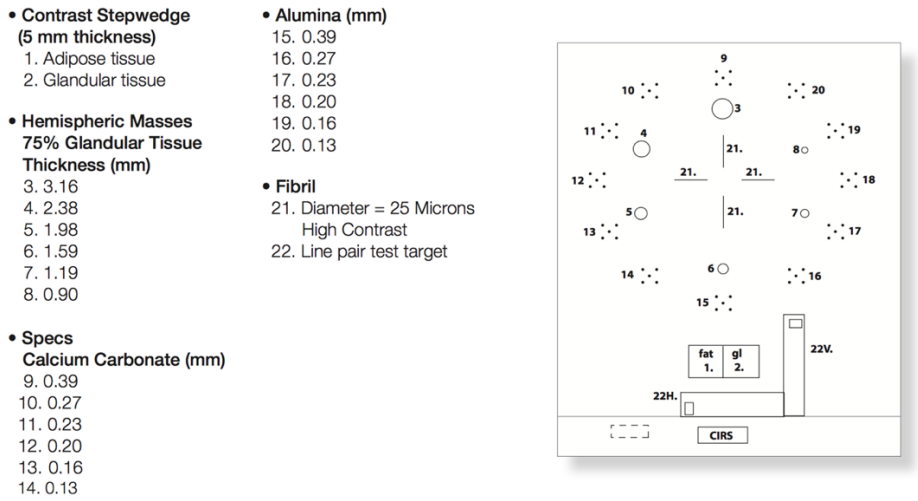

Figure 11: Details of the insert embedded in CIRS – 014AD [15]

2.2 Image acquisition and processing

The aim of this paragraph is to describe all the procedures done during the image acquisition. In the first part we will discuss about radiation dose because it is important to understand the connection between radiation dose and image quality. It is known that to improve image quality it is usually necessary to increase the radiation dose but there is a limitation due to patient safety.

In the second part, instead, it is described the phase retrieval algorithm used to get the phase map of our images.

2.1.1 Radiation dose

To evaluate the radiation dose to the phantom it is necessary to consider different factors as tube current, tube voltage, acquisition time, number of images and the material of the phantom.

The first step is the measurement of the air ESAK (Entrance Skin Air Kerma) using the equation:

$$ESAK = I \cdot t \cdot n \cdot T.O. \tag{26}$$

Where I (mA) is the tube current, t (s) the acquisition time for a single image, n the number of images acquired and T.O. (mGy/mAs) is the tube output.

The values of tube output are calculated using both the small focal spot and the large focal spot and the results are presented in table 2.

Large focal spot (50 µm)	Tube Voltage (kV)	T.O. (mGy/mAs) @500 mm
	80	0.404
	120	0.826
Small focal spot (7 µm)	80	0.356
	120	0.773

Table 2: Values of tube output are calculated using the small focal spot and the large focal spot

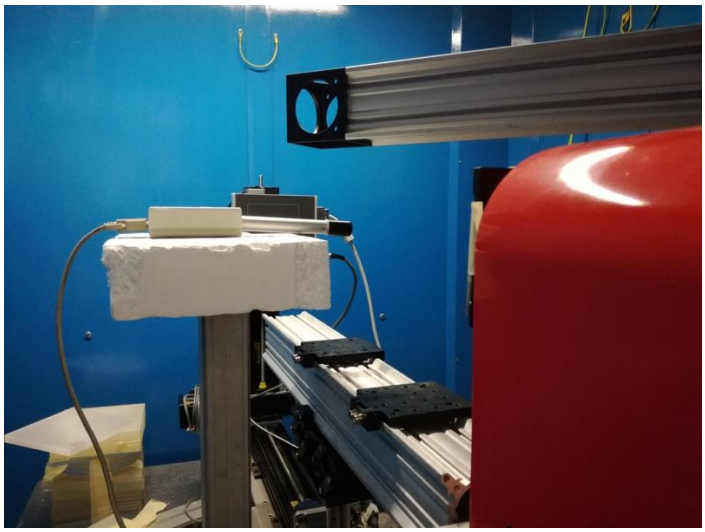

Figure 13: Experimental setup used to measure the tube output. The ionization chamber (Radcal corporation mod. 20X6-6) is placed at isocenter (500 mm from the source).

At this point we calculate ESAK values in two different cases: large focal spot and small focal spot.

The measures acquired using the large focal spot are taken fixing the tube current to 0.5 mA and using two different tube voltages 80 kV and 120 kV.

The acquisition time of our X-ray tube for a single image is 0.5 s so the ESAK values are:

Large focal spot	Tube current (mA)	Tube voltage (kV)	# images	Acquisition time (s)	T.O. (mGy/mAs)	ESAK (mGy)
	0.5	80	1	0.5	0.404	0.101
	0.5	120	1	0.5	0.826	0.207

Table 3: ESAK values calculated using the large focal spot.

The measures acquired using the small focal spot are taken at two different tube current and using the same voltage as in the previous case:

Small focal spot	Tube current (mA)	Tube voltage (kV)	# images	Acquisition time (s)	T.O. (mGy/mAs)	ESAK (mGy)
	0.1	80	1	0.5	0.356	0.018
	0.08	120	1	0.5	0.773	0.031

Table 4: ESAK values calculated using the small focal spot

Using the small focal spot is not possible to set the same tube current for the two values of tube voltage due to the specifications of the X-ray tube (figure 10).

It is known that a consequence of using small focal spot is reduced maximal tube current because the surface area of the anode hit by the electron beam is smaller and it is difficult to dissipate heat.

After ESAK it is necessary to calculate MGD (Mean Glandular Dose) values because in our study the phantom simulates breast tissue. For this reason we have to multiply the ESAK value for a specific coefficient called D_{gN} (Normalized Glandular Dose), the benchmark parameter useful to calculating the glandular dose in mammography.

In the last years the D_{gN} values are extended to high energy values because there is an increasing interest in dual energy mammography where the optimal beam energy is likely to ben very high (> 100 keV), well beyond clinical mammographic X-ray beam energy.

The D_{gN} values for these high energy X-ray beams may be useful for calculating glandular breast dose in general diagnostic radiographic studies or in computed tomographic studies, under specific assumptions.

In table 5 are reported the D_{gN} values corresponding to the tube voltage values used in this study. In table 6, instead, are reported the calculated ESAK values and the corresponding MGD for a single image under our experimental conditions.

50/50 breast tissue (5 cm thickness)	Tube voltage (kV)	DGN (mGy/mGy)
	80	0.939
	120	0.997

Table 5: D_{gN} values corresponding to the tube voltage values used in this study. [17]

In our case we want the D_{gN} values for breast tissue 50/50, so we have to take the two D_{gN} 0% and 100% glandular at the thickness and tube voltage considered and take the mean value (figure 14).

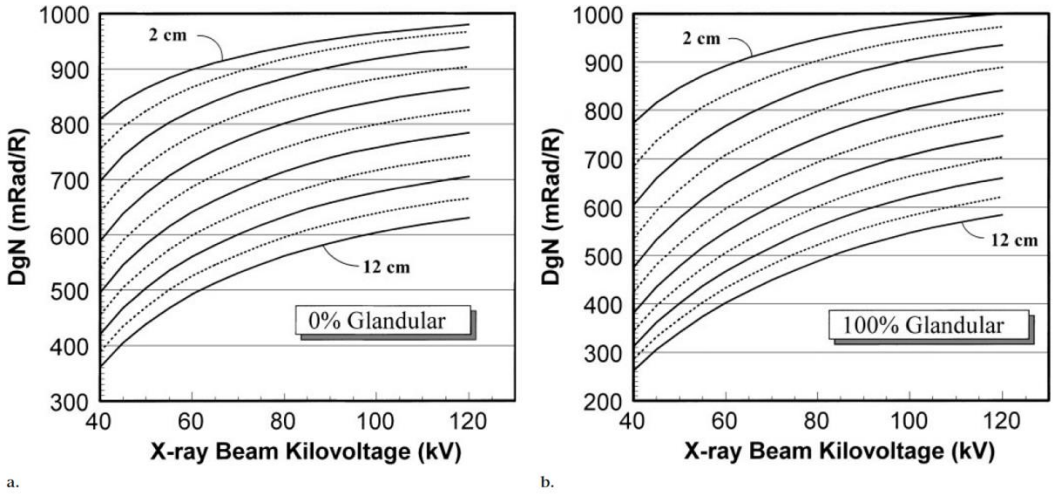

Figure 14: Graphs show D_{gN} values for conventional polyenergetic X-ray beams in which a tungsten anode and 2.5 mm of added aluminum filtration (our added filtration is 2.54 mm Al) are used. D_{gN} values are shown for (a) 0% glandular breasts and (b) 100% glandular breasts. D_{gN} values are expressed in milliard per roentgen. To convert to SI units (mGy/mGy), we have to multiply by $1/873$ [17].

CIRS-014AD			
	Tube voltage (kV)	**ESAK (mGy)**	**MGD (mGy)**
Large focal spot	80	0.101	0.095
	120	0.207	0.206
Small focal spot	80	0.018	0.017
	120	0.031	0.031

Table 6: Calculated ESAK values and the corresponding MGD for a single image under our experimental conditions.

The purpose of this study is to investigate the image quality for detection of simulated microcalcifications and masses in a breast phantom as a function of the radiation dose. For this reason, using the large focal spot, we take the running sum of 30 consecutive image frame and using the small focal spot, we take the running sum of 100 consecutive image frame. The MGD values are reported in table 7 and 8.

	Tube voltage (kV)	**MGD (mGy) for 30 images**
Large focal spot	80	2.845
	120	6.176

Table 7: MGD values for the sum of 30 images using the large focal spot

	Tube voltage (kV)	MGD (mGy) for 100 images
Small focal spot	80	1.670
	120	3.084

Table 8: MGD values for the sum of 100 images using the small focal spot.

2.1.2 ANKAphase: phase retrieval

To retrieve the phase map, we use ANKAphase an ImageJ plugin that process X-ray in line phase-contrast radiographs and reconstructs the projected thickness of the objects imaged in the radiographs. It uses the Paganin algorithm [13].

ANKAphase can be used with a series of radiographs taken in tomographic acquisition, so it can process a series of phase contrast images taken from different views.

The algorithm used in ANKAphase is valid under this conditions:

- The object imaged consist of a homogeneous material (constant density).
- The radiation is monochromatic.
- The distance between the object and the detector plane fulfils the near field conditions:

$$z \ll {}^{d^2}/_{\lambda} \tag{26}$$

where d is the size of the smallest feature in the object and λ is the X-ray wavelength.

In these conditions the intensity distribution I (x,y) measured at distance z between object and detector, can be used to retrieve the projected thickness t (x,y) of the object linked to δ and β values of the complex refractive index (see section 1.1.1).

It can be useful to consider the reconstructed phase map φ (x,y) rather than the projected thickness because the thickness is not useful considering the density variations in the material. In φ (x,y) there is the ratio ${}^{\delta}/_{\beta}$ as input parameter and this is useful when the values of δ and β are not known. In addition to this, ${}^{\delta}/_{\beta}$ ratio is useful when the chemical composition of the material is not well known and it is possible that in the entire object the values of δ and β are non constant but their ratio remains unvaried.

2.1.3 δ and β coefficients

The complex refractive index is:

$$n = 1 - \delta + i\beta$$

where δ is the decrement from unity of the X-ray refractive index of the object material and β is the imaginary part.

The quantities β and μ are related:

$$\mu = \frac{4\,\pi\,\beta}{\lambda} \tag{27}$$

Instead the wave phase shift crossing a material thickness d along z direction is:

$$\phi\,(x,y) = -\frac{2\pi}{\lambda}\int_0^d \delta(x,y,z)\,dz \tag{28}$$

If we assume that $\delta(x,y,z)$ is constant:

$$\delta = -\frac{\lambda}{2\pi}\,\frac{\phi(x,y)}{d} \tag{29}$$

where $\phi(x,y)$ is in radiant and d in mm.

δ and β values are derived from CSIRO CSS website [18] for 50/50 breast tissue at the average energies of 39 keV and32 keV for the 120 kV and 80 kV beam energies respectively.

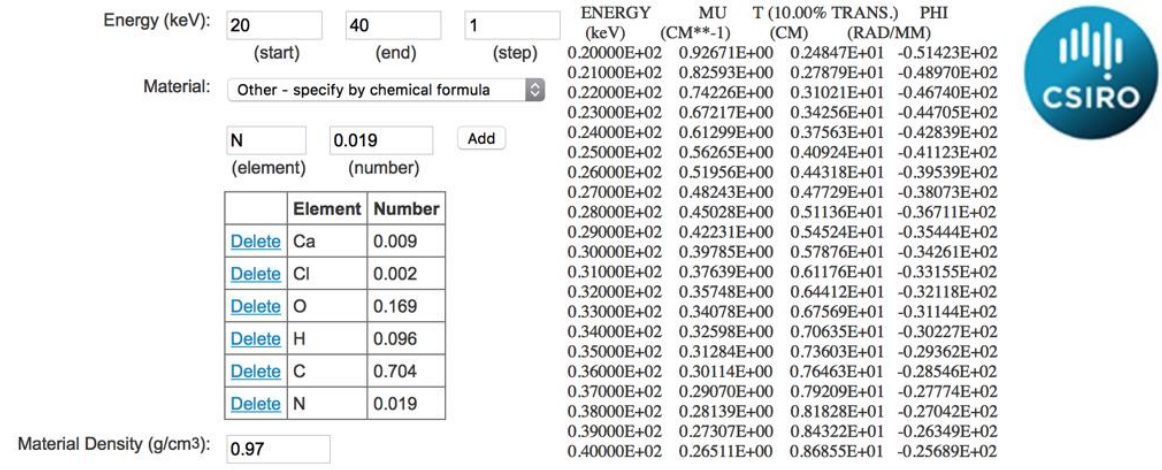

Figure 15: Values of energy, attenuation coefficient, thickness and PHI (rad/mm) taken from CSIRO CSS website. These values are obtained inserting the chemical composition of our phantom [18].

Tube voltage (kV)	Effective energy (keV)	λ (m) $\times 10^{-12}$ m	δ $\times 10^{-7}$	PHI (rad/mm)	β $\times 10^{-11}$	$\frac{\delta}{\beta}$	μ (cm^{-1})
80	32	3.68	1.98	320	8.31	2378	0.357
120	39	3.12	1.98	260	8.42	2347	0.273

Table 9: Calculated values of λ, δ and β using (27) and (29).

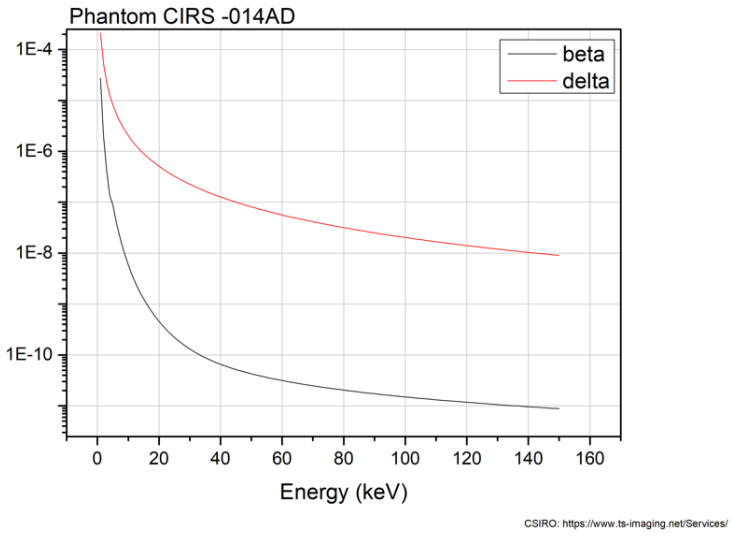

Figure 16: Calculated values of the refractive index for our phantom CIRS-014AD.

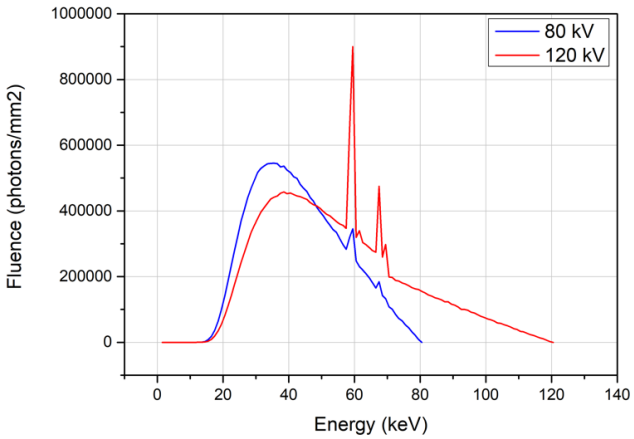

Figure 17: Energy spectrum at 80 kV and 120 kV, using an added filtration of 2.54 mm Al.

2.3 Laboratory measurements

The experimental work of this thesis was carried out in the laboratory of medical physics of this department using a scanner for micro CT dedicated to the breast. The micro-focal spot of this scanner, together with a sufficient distance between source and object, produces an X-ray beam with a sufficient spatial coherence. The aim of this work was to investigate the characteristics of propagation–based phase–contrast imaging in showing microcalcifications and soft tissue lesions. In this paragraph we will present the images acquired and the results of the corresponding analysis.

2.3.1 Absorption-based 2D imaging

In the first part of the experimental work we worked with a source to object distance of $R_1 = 500\ mm$, with a magnification of $M = 1.22$ (figure 18). In these conditions the contrast of the image is given by the attenuation of the X-ray beam in crossing the phantom.

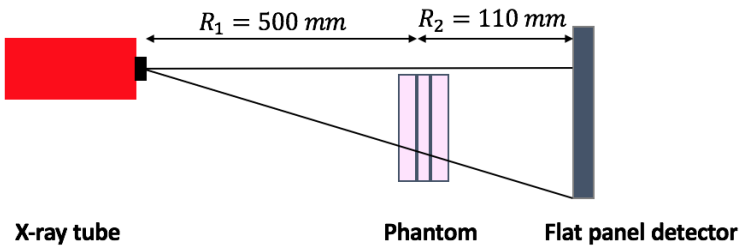

Figure 18: Schematic representation of the experimental setup used for absorption based imaging.

Each radiogram (I) is normalized to the FLAT field (F) after subtracting the DARK field (D), using the equation:

$$I_{Corr} = \frac{I - D}{F - D} \tag{30}$$

where the dark field was obtained with the source turned off and the flat image as an image obtained with the beam on but without the phantom. Using the large focal spot (50 μm), we acquired 30 images and the final image is the sum of 30 radiograms. Radiograms were acquired in two different configurations which are reported in table 10, including the dose values.

Large focal spot	Tube voltage (kV)	Tube current (mA)	Dose (mGy) 30 images
	120	0.5	6.176
	80	0.5	2.845

Table 10: Tube voltages, tube currents and dose values used to acquire images in absorption imaging, using the large focal spot.

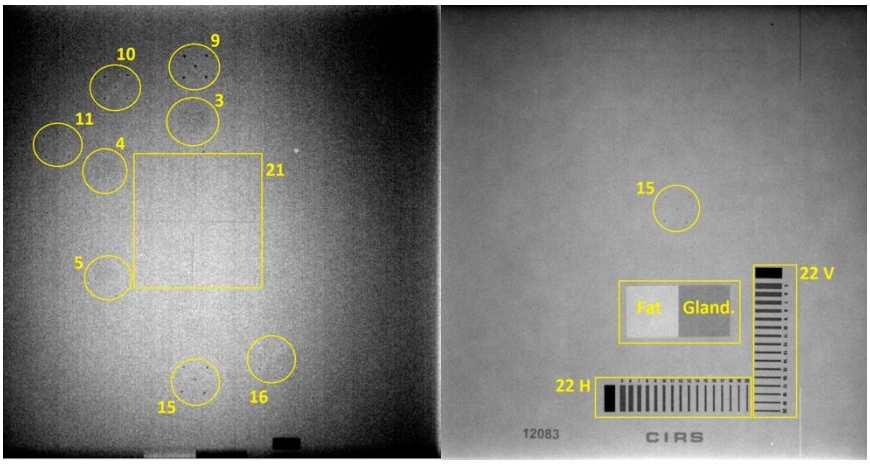

(a)

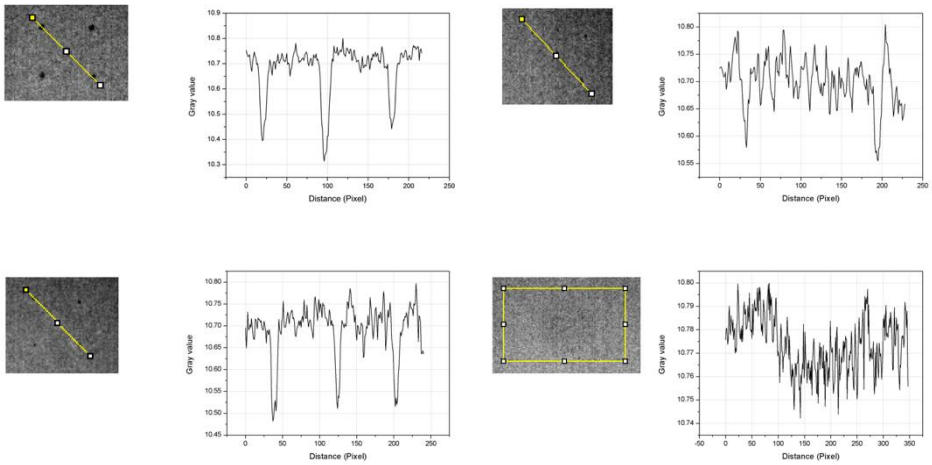

(b)

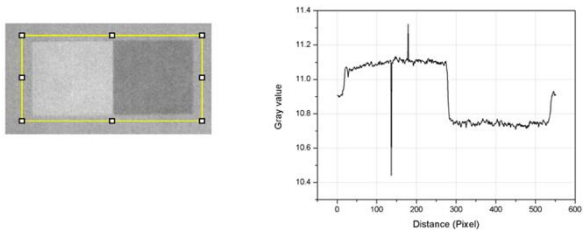

(c)

Figure 19: (a) attenuation-based radiograph of CIRS-014AD phantom (upper part and lower part), sum of 30 radiograms. The numbers of the elements in the circles are referred to figure 11. (b), (c) analysis of the details embedded in the phantom. The images were acquired at 80 kV, 0.5 mA, 15 s and 2.54 mm Al filter.

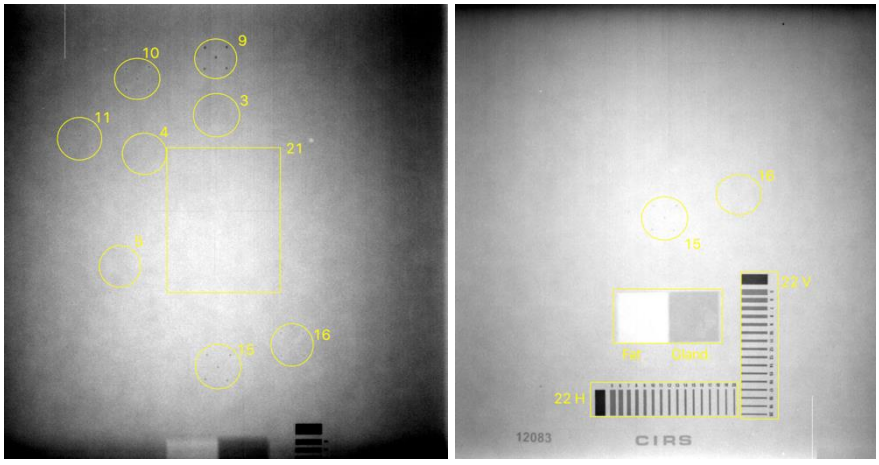

(a)

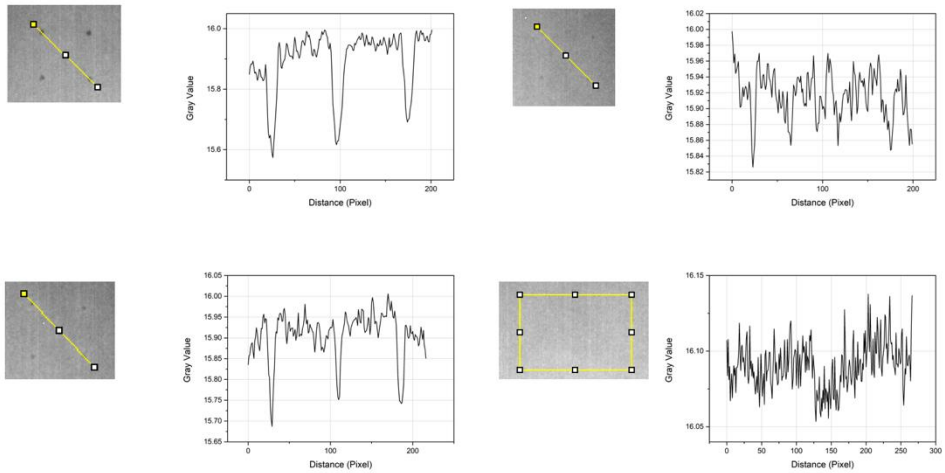

(b)

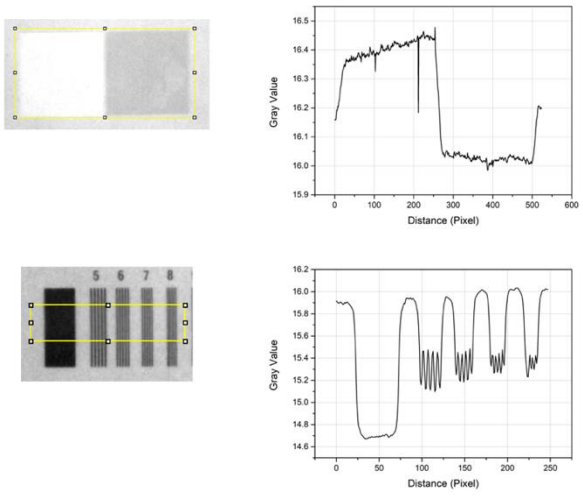

(c)

Figure 20: (a) attenuation-based radiograph of CIRS-014AD phantom (upper and lower part), sum of 30 radiograms. The numbers of the elements in the circles are referred to figure 11. (b), (c) Analysis of the details embedded in the phantom. The images were acquired at 120 kV, 0.5 mA, 15 s and 2.54 mm Al filter.

Analyzing the images 19 and 20, we can see that in attenuation-based imaging, both at 80 kV and 120 kV, we can recognize 3 masses out of 6. In particular, we see the three biggest masses: mass #3 with 3.16 mm thickness, mass #4 with 2.38 mm thickness and mass #5 with 1.98 mm thickness.

Analyzing the microcalcifications (specs, see figure 11), instead, we can recognize 5 specs out of 12. From specs 9 to 11 the composition is of calcium carbonate and their diameter is 0.39, 0.27 and 0.23 respectively. Specs 15 and 16, instead, are made up of Alumina and their diameter is 0.39 and 0.27 respectively.

Observing the profiles of the details embedded in the phantom (b and c, figure 19 and 20) we see some vertical lines because of some lines of the detector that are composed of defective pixels.

Using the small focal spot (7 μm), instead, we acquired 100 images and the final image is the sum of 100 radiograms. Radiograms were acquired in two different configurations, which are reported in table 11, including the dose values.

Small focal spot	**Tube voltage (kV)**	**Tube current (mA)**	**Dose (mGy) 100 images**
	120	0.08	3.084
	80	0.1	1.670

Table 11: Tube voltages, tube currents and dose values used to acquire images in absorption imaging using the small focal spot.

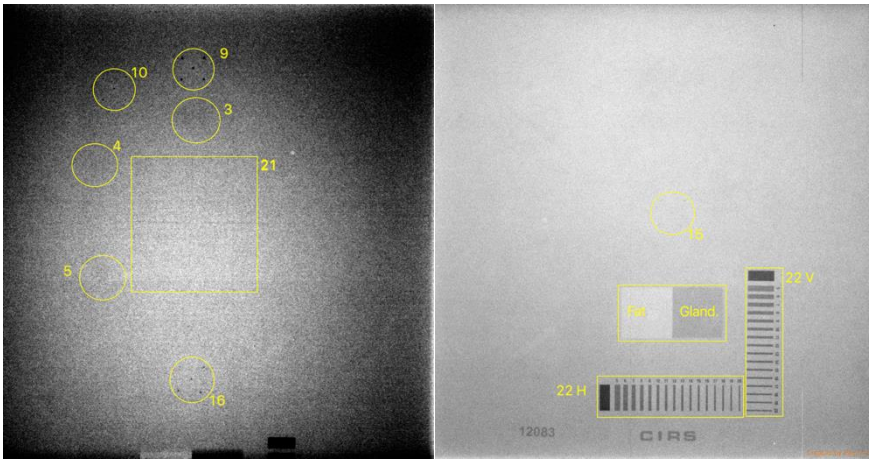

(a)

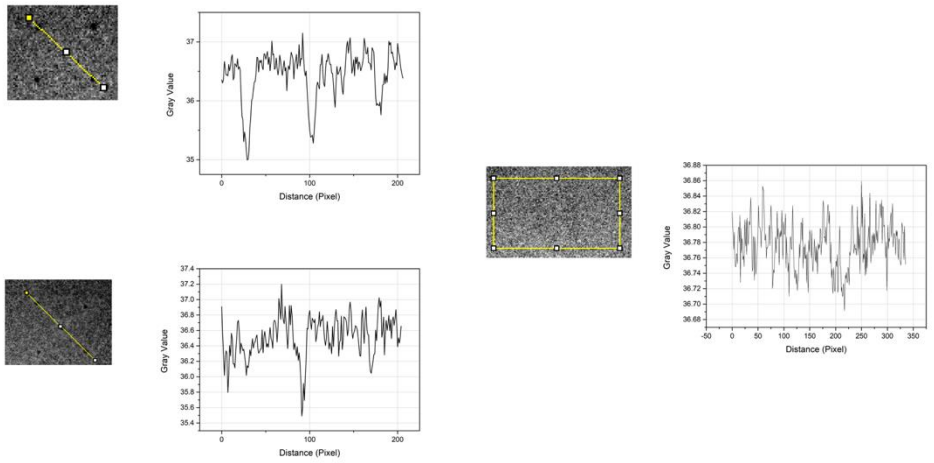

(b)

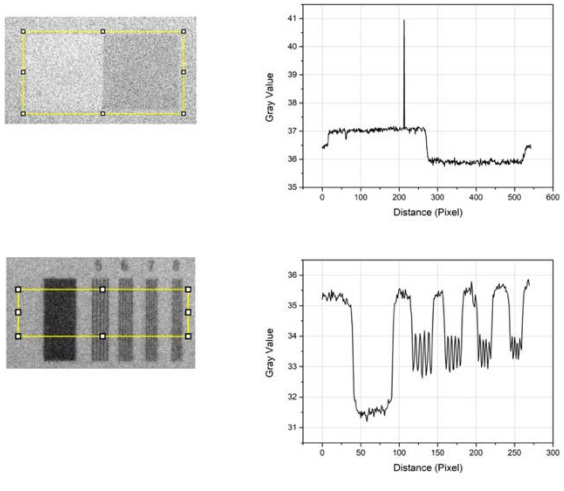

(c)

Figure 21: (a) attenuation-based radiograph of CIRS-014AD phantom (upper and lower part), sum of 100 radiograms. The numbers of the elements in the circles are referred to figure 11. (b) (c) analysis of the details embedded in the phantom. The images were acquired at 80 kV, 0.1 mA, 50 s and 2.54 mm Al filter.

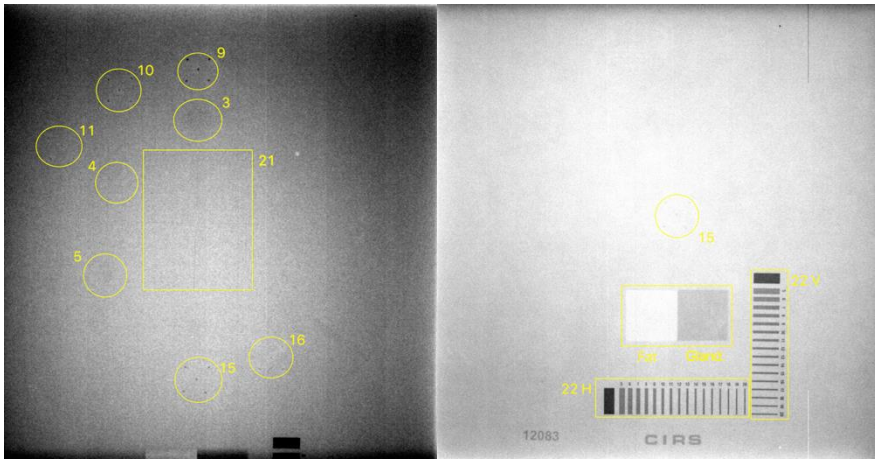

(a)

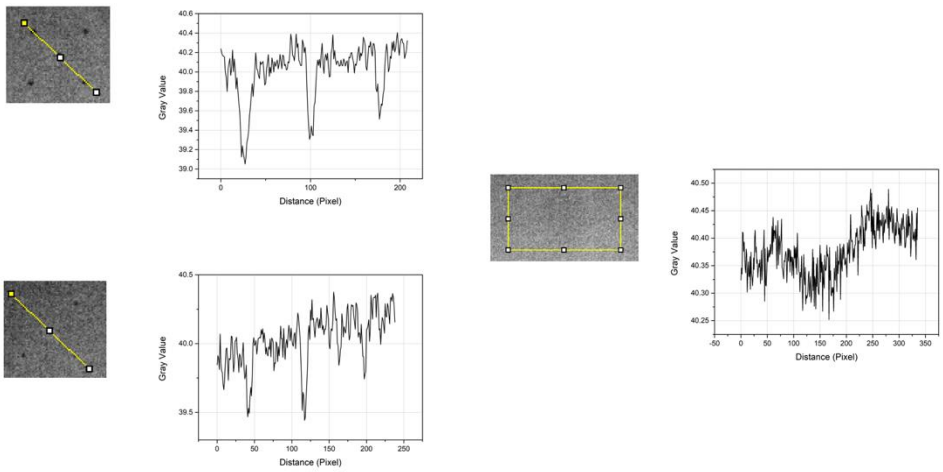

(b)

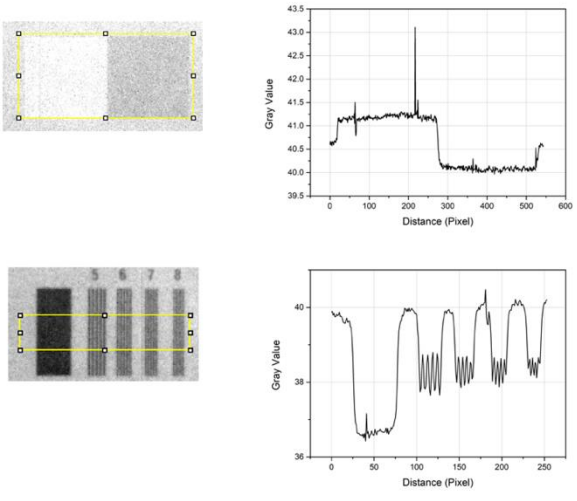

(c)

Figure 22: (a) attenuation-based radiograph of CIRS-014AD phantom (upper and lower part), sum of 100 radiograms. The numbers of the elements in the circles are referred to figure 11. (b), (c) analysis of the details embedded in the phantom. The images were acquired at 120 kV, 0.08 mA, 50 s and 2.54 mm Al filter.

Analyzing the images 21 and 22, we can see that in attenuation-based imaging, both at 80 kV and 120 kV, we can recognize 3 masses out of 6 as in the previous case. In particular, we see the three biggest masses.

Analyzing the microcalcifications (specs, see figure 11), instead, the images are different between 80 kV and 120 kV because using the highest voltage we can recognize 5 specs out of 12. At 80 kV, instead, only 3 specs out of 12.

Observing the profiles of the details embedded in the phantom (b and c, figure 21 and 22) we see some vertical lines because of some lines of the detector that are composed of defective pixels and the correction for flat field and dark field was not effective at all.

2.3.2 Propagation-based phase-contrast and phase retrieval 2D imaging

In this second part, we worked fixing the source-to-object distance ($R_1 = 500\,mm$) and varying the source-to-image distance ($R_1 + R_2 = 1015\,mm$), with a magnification of $M = 2.03$ (figure 27).

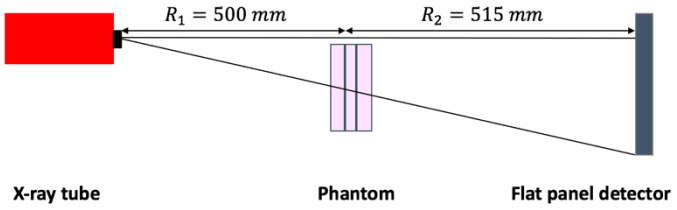

Figure 23: Schematic representation of the experimental setup used for propagation-based phase-contrast imaging

A sample-to-detector distance is introduced for the development of interference pattern onto the imaging plane.

The phase modulation of the emerging beam is transformed into amplitude modulation due to free-space propagation of the X-ray beam passing trough the object. Contrast is generated from beam attenuation and, in part, from the interference between parts of the emerging wave fronts that have experienced different phase shift. This last kind of contrast is superimposed onto the attenuation contrast and helps to improve the visibility of the borders or details. In particular, our in-line phase-sensitive approach is the simplest because does not involve the

presence of any optical devices between the sample and the detector. Each radiogram was corrected for the dark field and the flat field using equation (30).

Using the large focal spot (50 μm), we acquired 30 images and the final image is the sum of 30 radiograms. Radiograms were acquired in two different configurations which are reported in the previous table 10, including the dose values.

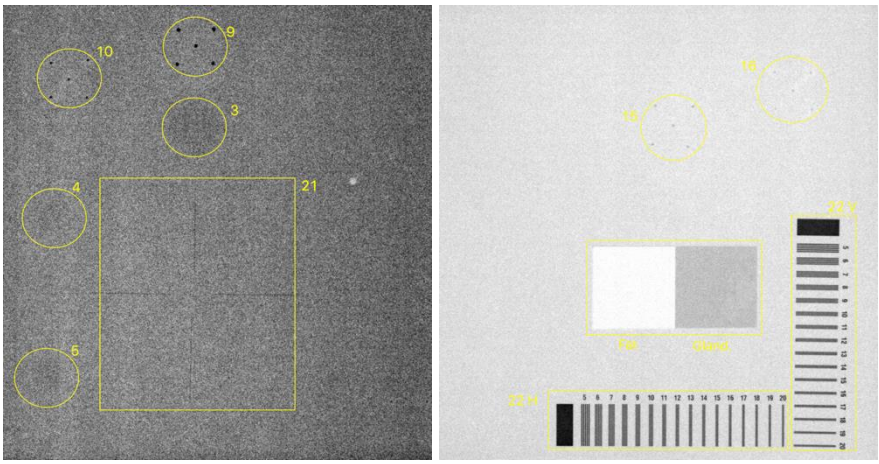

(a)

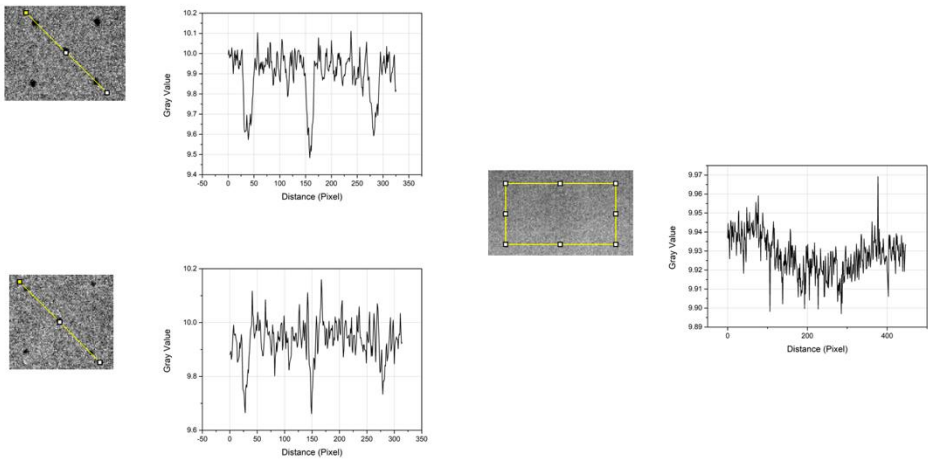

(b)

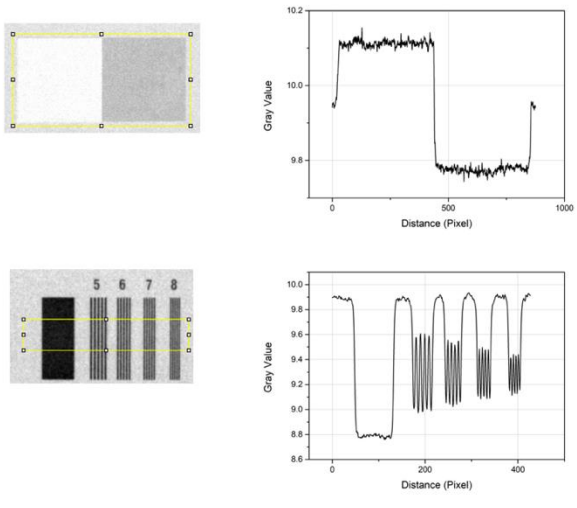

(c)

Figure 24: (a) propagation-based phase-contrast radiograph of CIRS-014AD phantom (upper and lower part), sum of 30 radiograms. The numbers of the elements in the circles are referred to figure 11. (b), (c) analysis of the details embedded in the phantom. The images were acquired at 80 kV, 0.5 mA, 15 s and 2.54 mm Al filter.

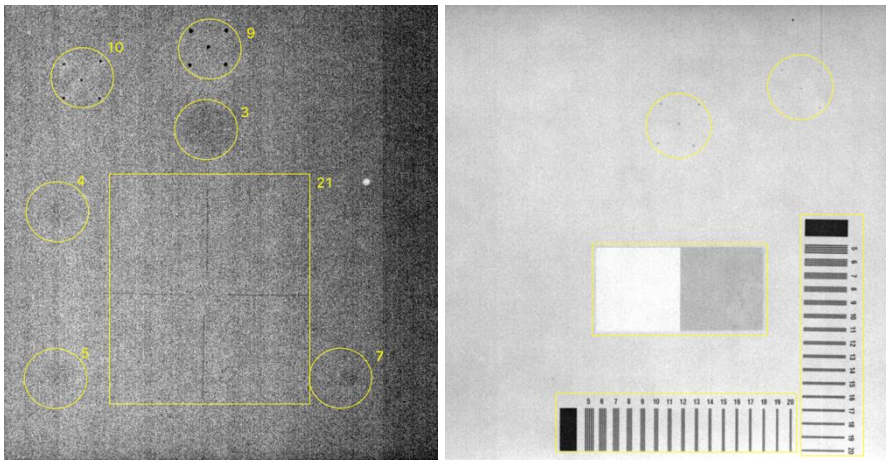

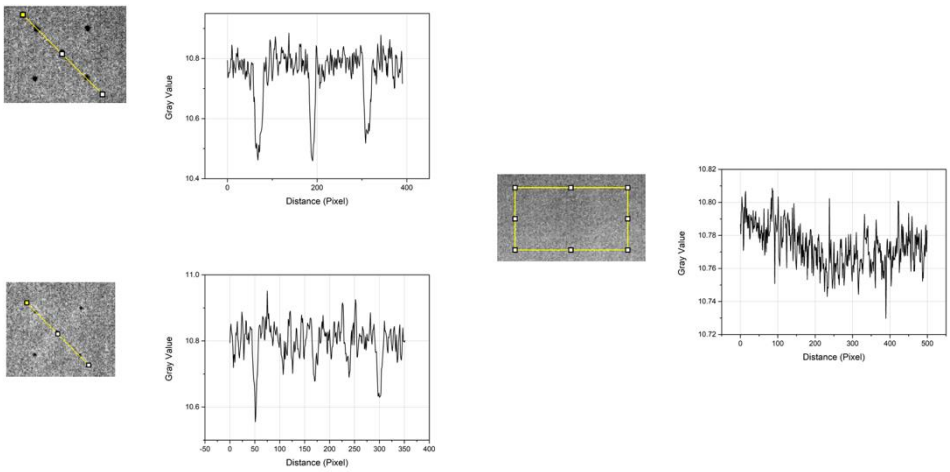

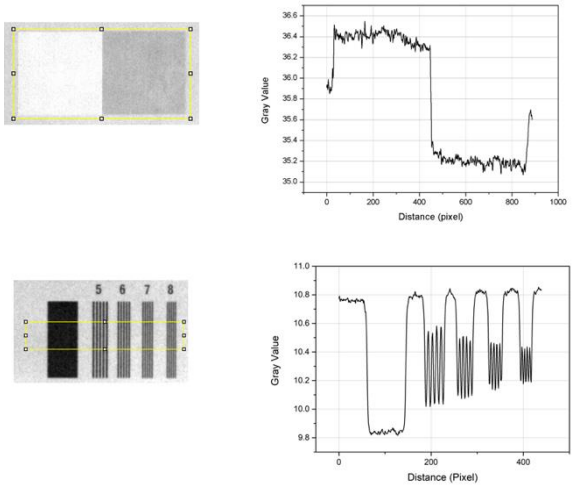

Figure 25: (a) propagation-based phase-contrast radiograph of CIRS-014AD phantom (upper and lower part), sum of 30 radiograms. The numbers of the elements in the circles are referred to figure 11. (b), (c) analysis of the details embedded in the phantom. The images were acquired at 120 kV, 0.5 mA, 15 s and 2.54 mm Al filter.

Analyzing the images 24 and 25, we can see that in phase-contrast imaging, at 120 kV, we can recognize 4 masses out of 6 so there is a great improvement in image and this confirm our hypothesis that using higher energy it is possible to see more details in the image.

Due to magnification, instead, not all the microcalcifications seen in the previous case (attenuation-based) are showed.

Using the small focal spot (7 μm), instead, we acquired 100 images and the final image is the sum of 100 radiograms. Radiograms were acquired in two different configurations which are reported in the previous table 11, including the dose values.

In this case, observing images 26 and 27, there is an improvement in image visibility for higher energy images. At 80 kV, instead, we cannot see masses because of the low tube current values and the reduced X-ray flux.

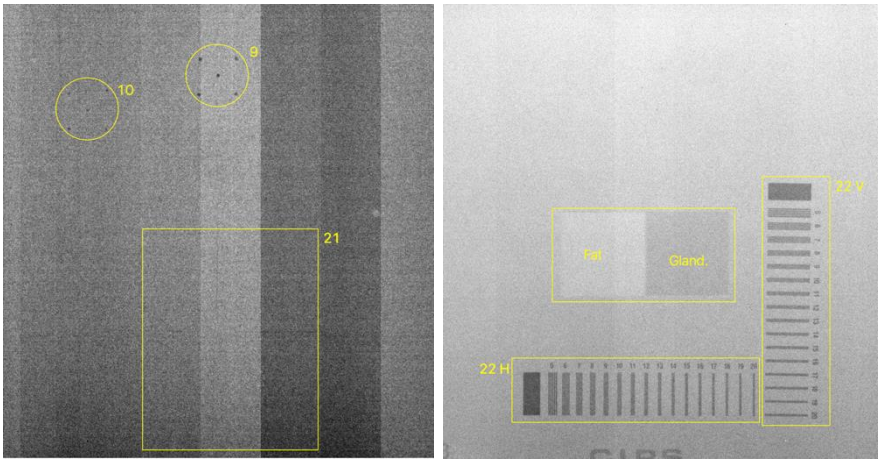

(a)

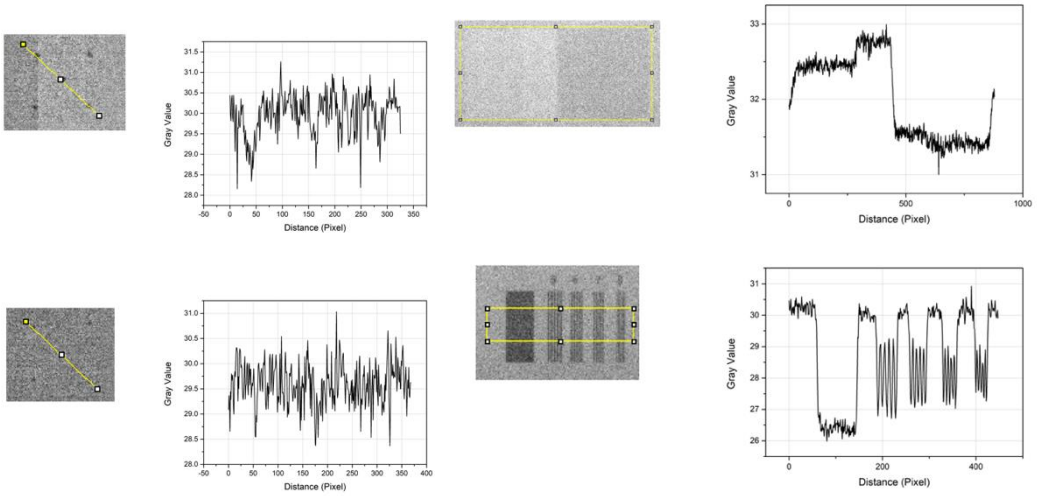

(b)

Figure 26: (a) propagation-based phase-contrast radiograph of CIRS-014AD phantom (upper and lower part), sum of 100 radiograms. The numbers of the elements in the circles are referred to figure 11. (b) analysis of the details embedded in the phantom. The images were acquired at 80 kV, 0.1 mA, 50 s and 2.54 mm Al filter.

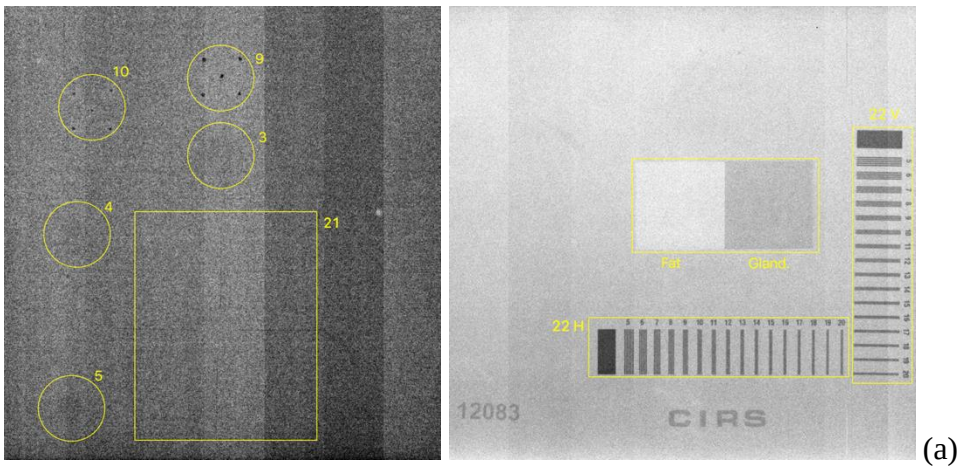

(a)

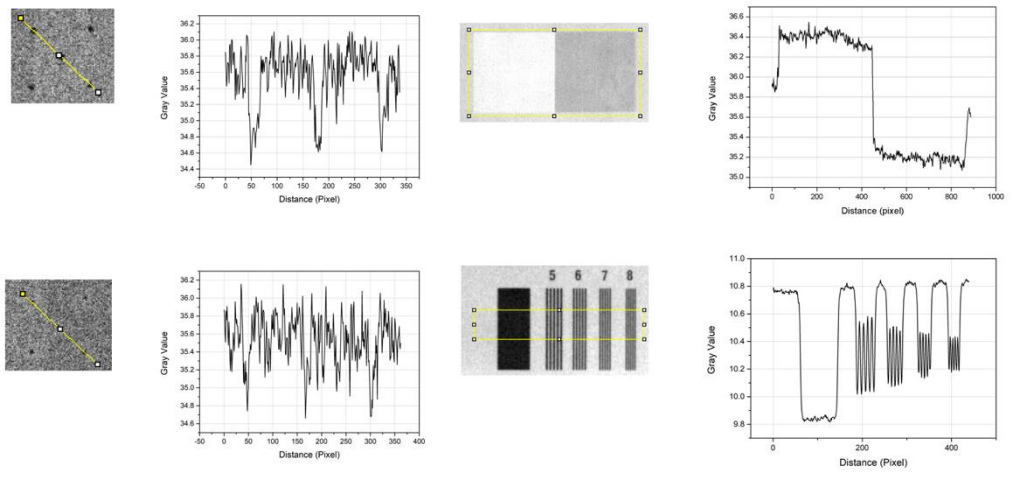

(b)

Figure 27: (a) propagation-based phase-contrast radiograph of CIRS-014AD phantom (upper and lower part), sum of 100 radiograms. The numbers of the elements in the circles are referred to figure 11. (b) analysis of the details embedded in the phantom. The images were acquired at 120 kV, 0.08 mA, 50 s and 2.54 mm Al filter.

In order to exhibit the phase-contrast of the details embedded in the phantom, the phase map must be retrieved from its phase contrast projection. To retrieve the phase map we use Paganin's algorithm (par. 1.6). In figures 28-29 there is a comparison between the images acquired at 120 kV and 80 kV using both large and small focal spot and in the next subparagraph there is the comparison between the three imaging configuration used in order to understand their effectiveness.

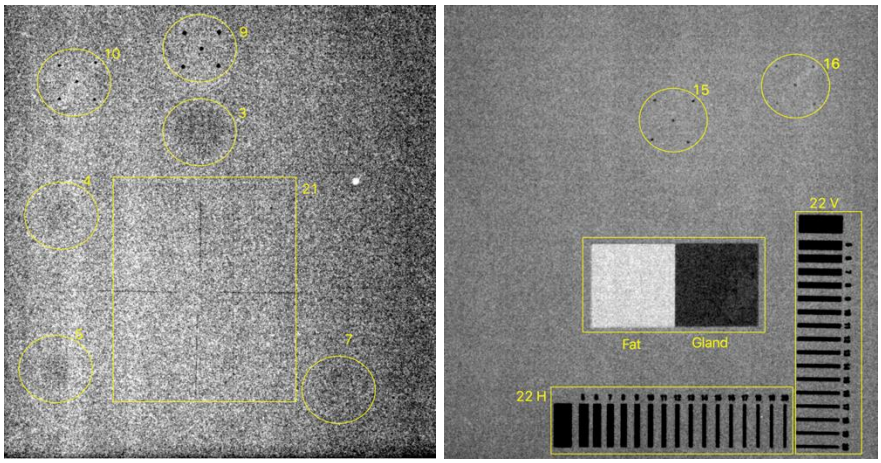

a)

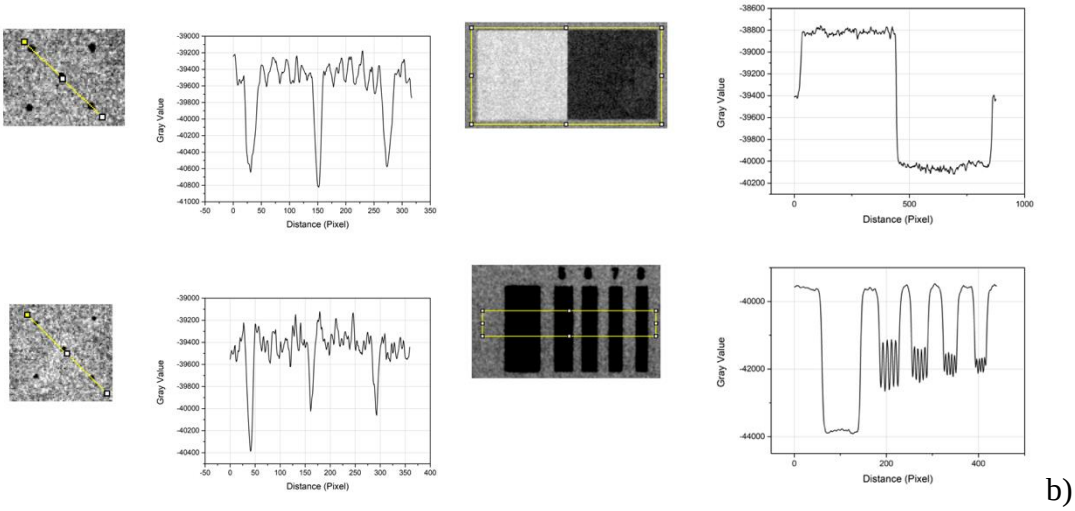

b)

Figure 28: (a) phase map of CIRS-014AD phantom (upper and lower part), sum of 30 radiograms. The numbers of the elements in the circles are referred to figure 11. (b) analysis of the details embedded in the phantom. The images were acquired at 80 kV, 0.5 mA, 15 s and 2.54 mm Al filter.

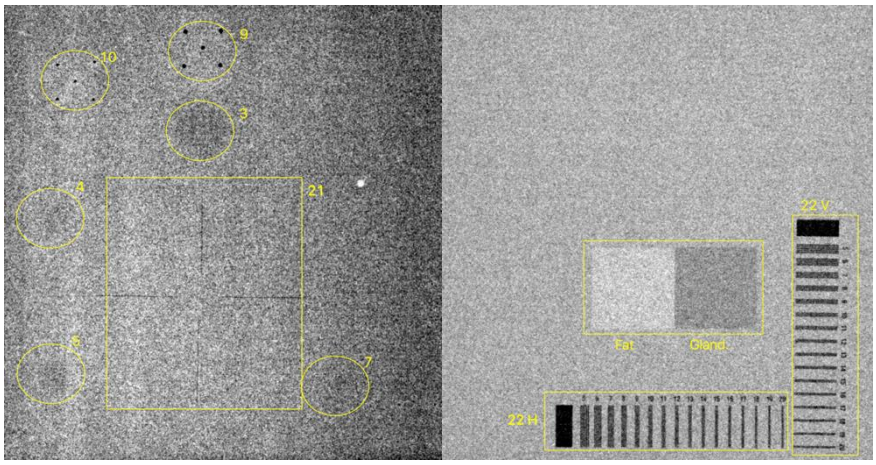

(a)

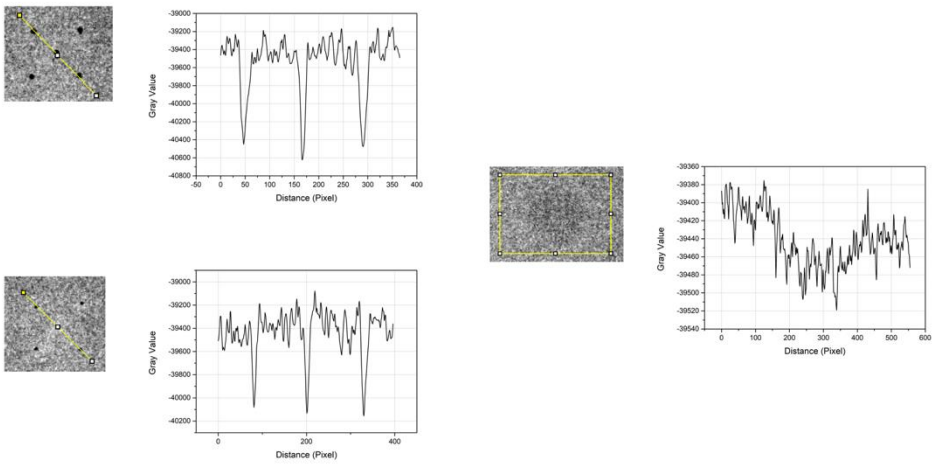

(b)

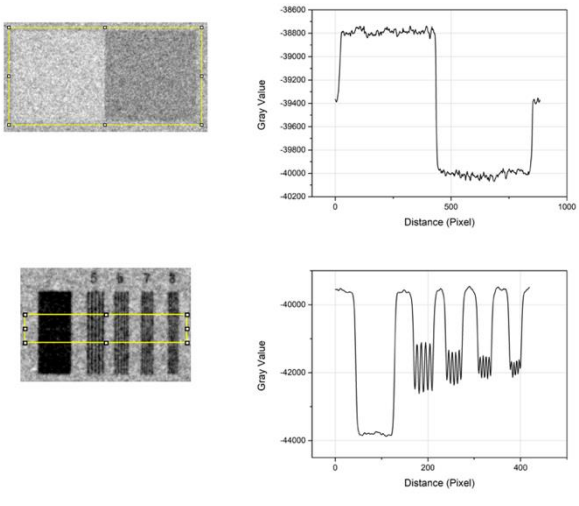

(c)

Figure 29: (a) phase map of CIRS-014AD phantom (upper and lower part), sum of 30 radiograms. The numbers of the elements in the circles are referred to figure 11. (b), (c) analysis of the details embedded in the phantom. The images were acquired at 120 kV, 0.5 mA, 15 s and 2.54 mm Al filter.

Using the small focal spot (7 μm), instead, we acquired 100 images and the final image is the sum of 100 radiograms. Radiograms were acquired in two different configurations which are reported in the previous table 11, including the dose values.

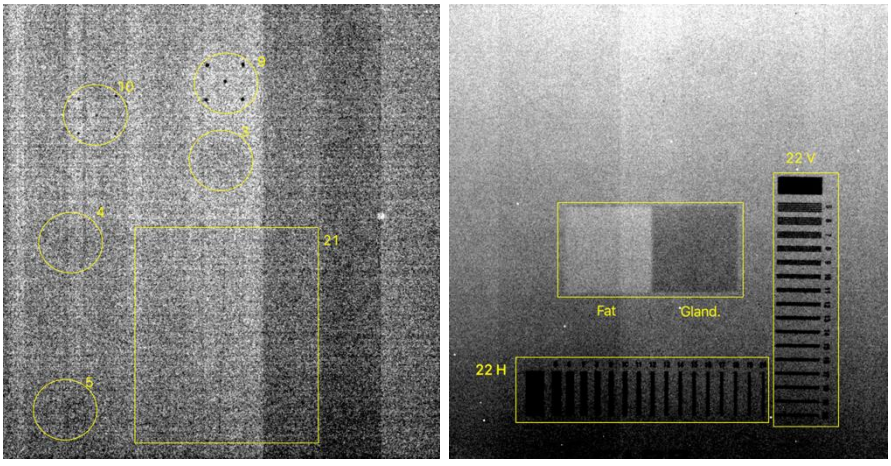

(a)

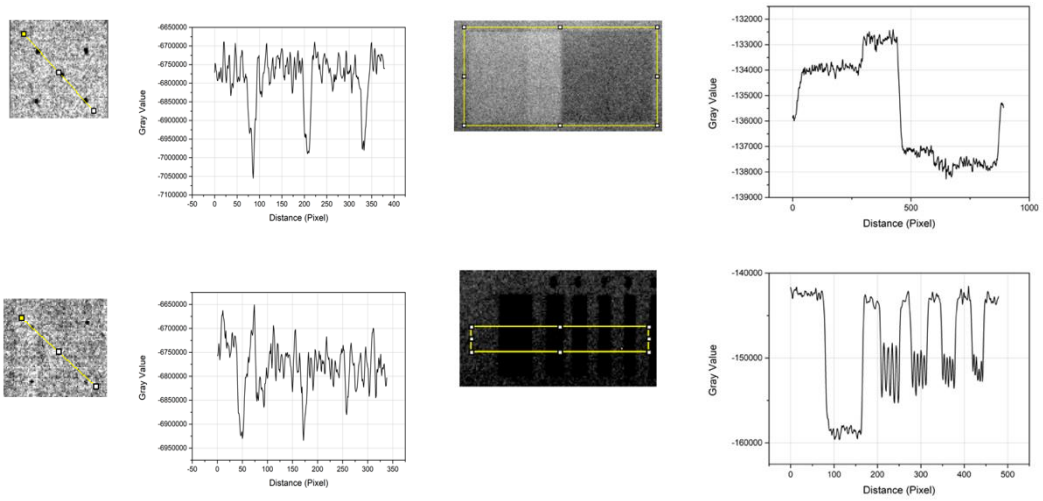

(b)

Figure 30: (a) phase map of CIRS-014AD phantom (upper part), sum of 100 radiograms. The numbers of the elements in the circles are referred to figure 11. (b) analysis of the details embedded in the phantom. The images were acquired at 80 kV, 0.1 mA, 50 s and 2.54 mm Al filter.

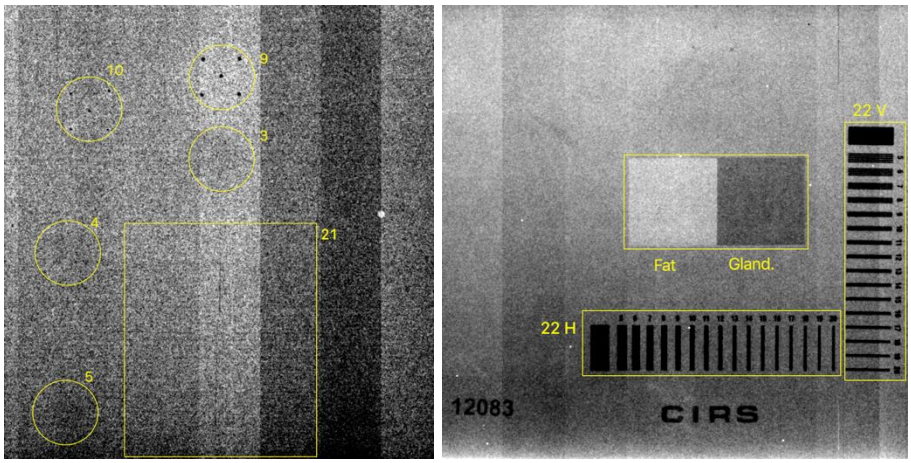

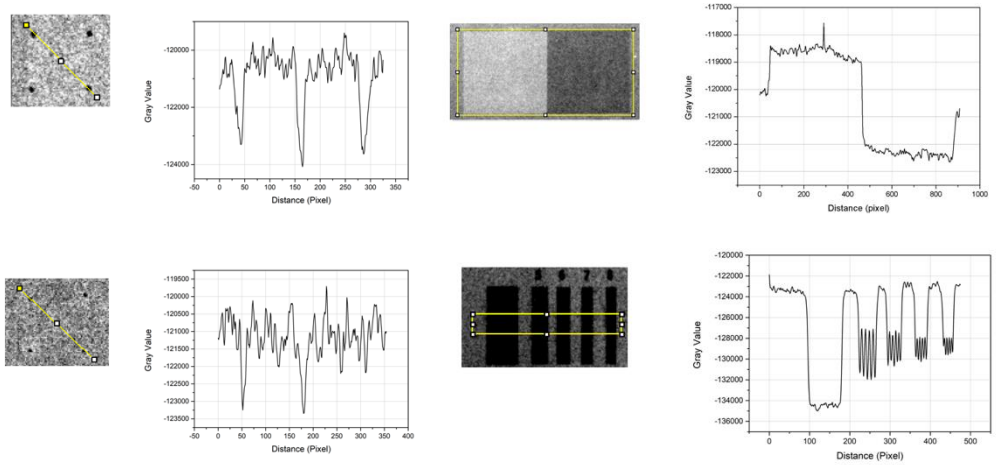

Figure 31: (a) phase map of CIRS-014AD phantom (upper part), sum of 100 radiograms. The numbers of the elements in the circles are referred to figure 11. (b) analysis of the details embedded in the phantom. The images were acquired at 120 kV, 0.08 mA, 50 s and 2.54 mm Al filter.

Retrieving the phase map of the images it is easier to recognize the masses and the microcalcifications because of the edge enhancement. One can see from previous figures that the details offer a much stronger signal with the phase retrieved image as compared to the two opposing images. It is worth to mention that the boundaries of the disks are sharper with the phase retrieved image. It is a well-known fact that with the employment of geometric magnification in clinical radiology, the boundaries of tissues are obscured due to the blurring caused by the finite focal spot size of the x-ray tubes.

Indeed, in the next paragraph there is a comparison between the three image techniques and it is showed that there is an improvement in the image quality using the small focal spot for phase images.

2.3.3 Results of 2D imaging

In order to have a quantitative comparison of the three different imaging methods, we calculated image quality parameters such as contrast-to-noise ratio (CNR) and signal-to-noise ratio (SNR) of the masses in the phantom. CNR and SNR are defined as:

$$CNR = \frac{I_O - I_I}{\sqrt{\frac{(\sigma_O^2 + \sigma_I^2)}{2}}} \tag{31}$$

$$SNR = \frac{I_I}{\sigma_I} \tag{32}$$

where I_O denotes the mean pixel value of the mass target averaged over a region of interest (ROI), I_I is the mean pixel value of the background averaged over a ROI of the same size and σ_I and σ_O are the corresponding pixel value variances. All the ROIs have the same size.

Since the CNR depends on the radiation dose, and in case of quantum-noise limited imaging it increases with the square root of the radiation dose, we used also the dose- normalized CNR as a parameter that is independent of the radiation dose, in order to characterize the performance of an imaging method for imaging at different doses. We defined the CNRD as:

$$CNRD = \frac{CNR}{\sqrt{D}} \tag{33}$$

The CNR for X-ray quantum limited detectors is related to $\sqrt{D}$, so dividing the CNR by $\sqrt{D}$, we can obtain a value related to the exposure level.

In order to compare the three imaging configurations (absorption-based, phase-contrast and phase), we show the results obtained in detection of the mass #3 (see figure 11) and in detection of glandular tissue (see figure 11), both using the large and the small focal spot, for two different values of tube voltage.

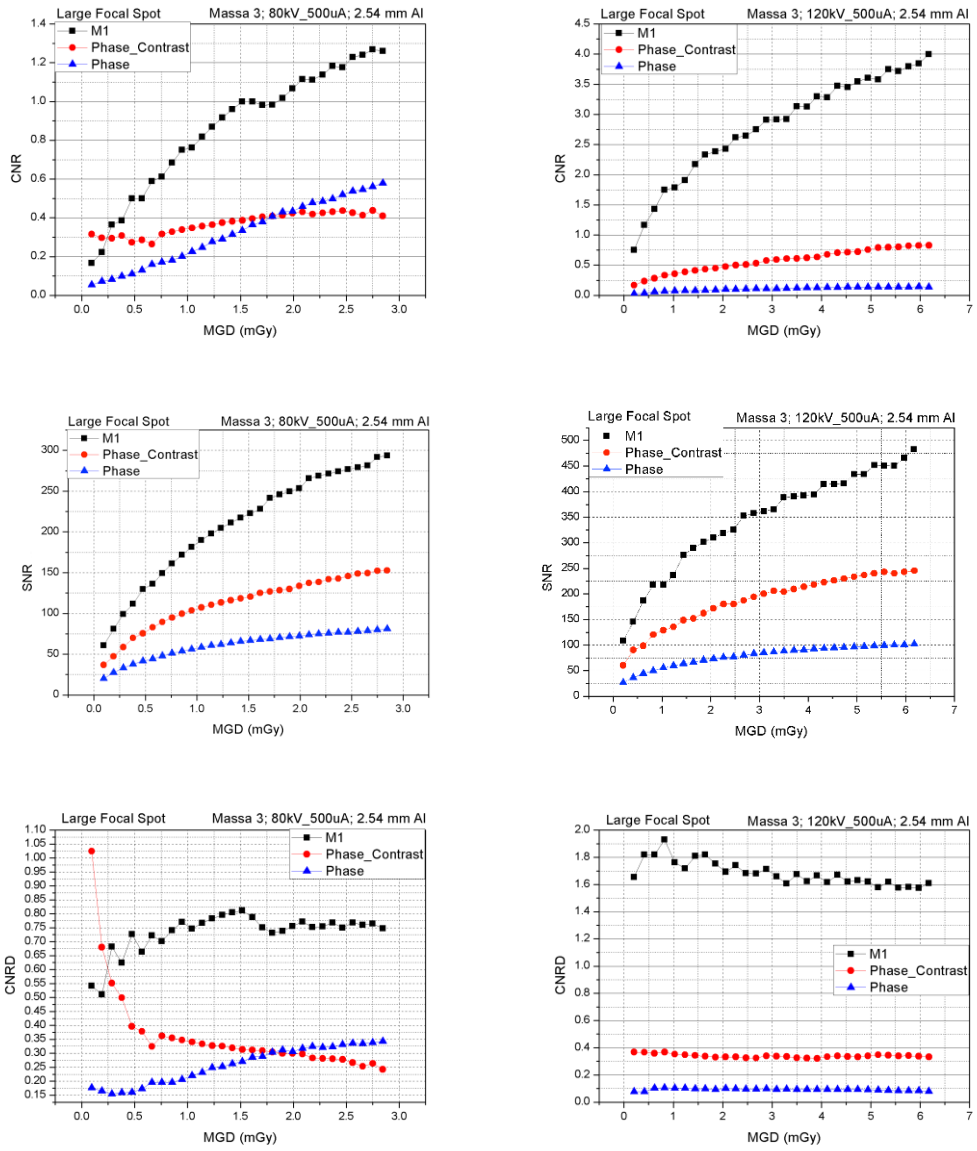

Figure 32: Values of CNR, SNR and CNRD obtained in detecting mass #3, using the large focal spot for two different tube voltages.

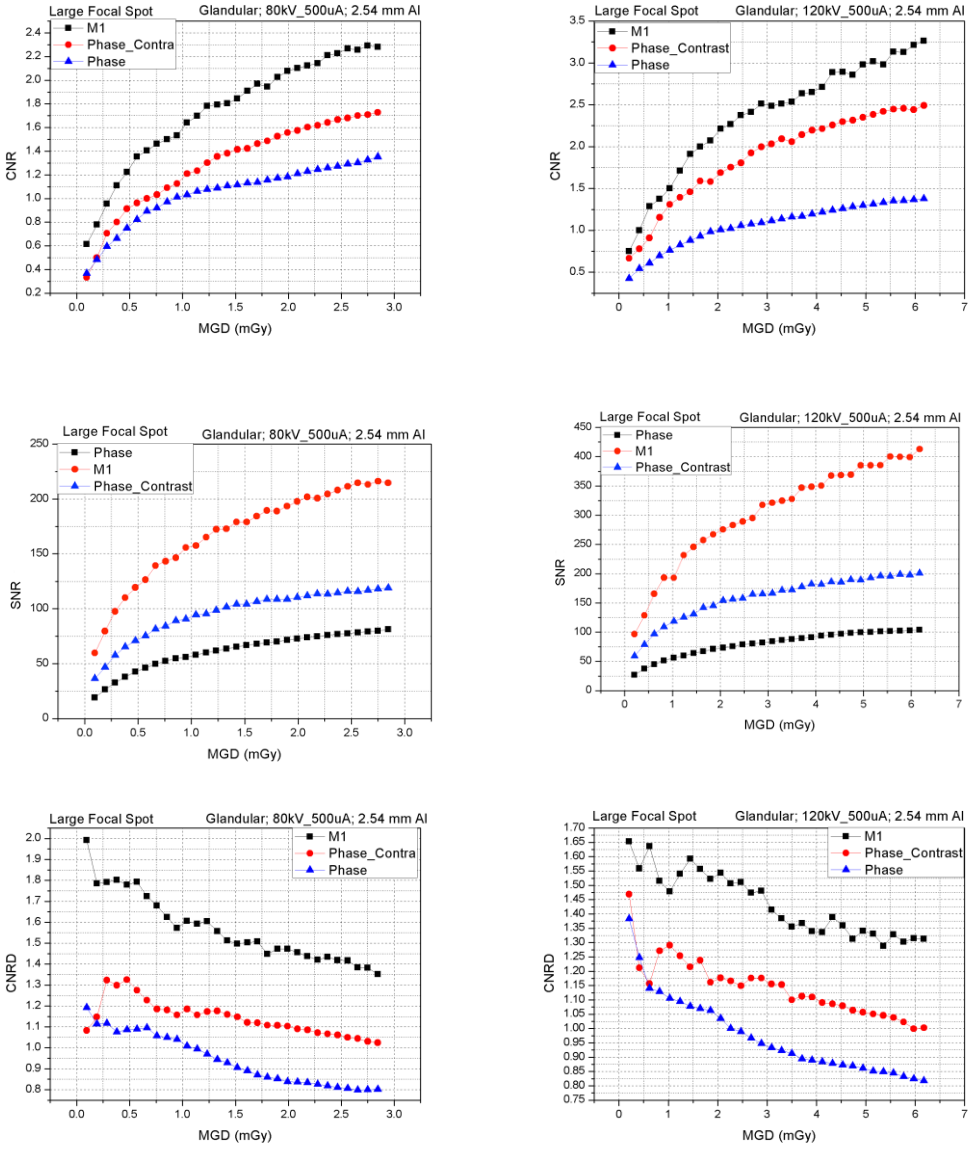

Figure 33: Values of CNR, SNR and CNRD obtained in detecting glandular tissue, using the large focal spot for two different tube voltages.

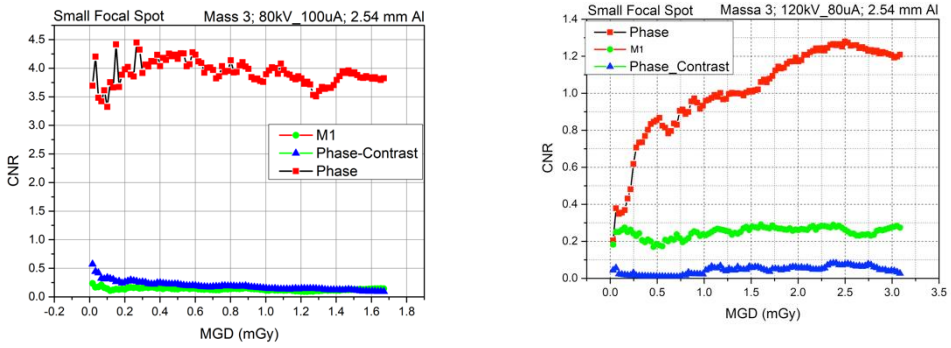

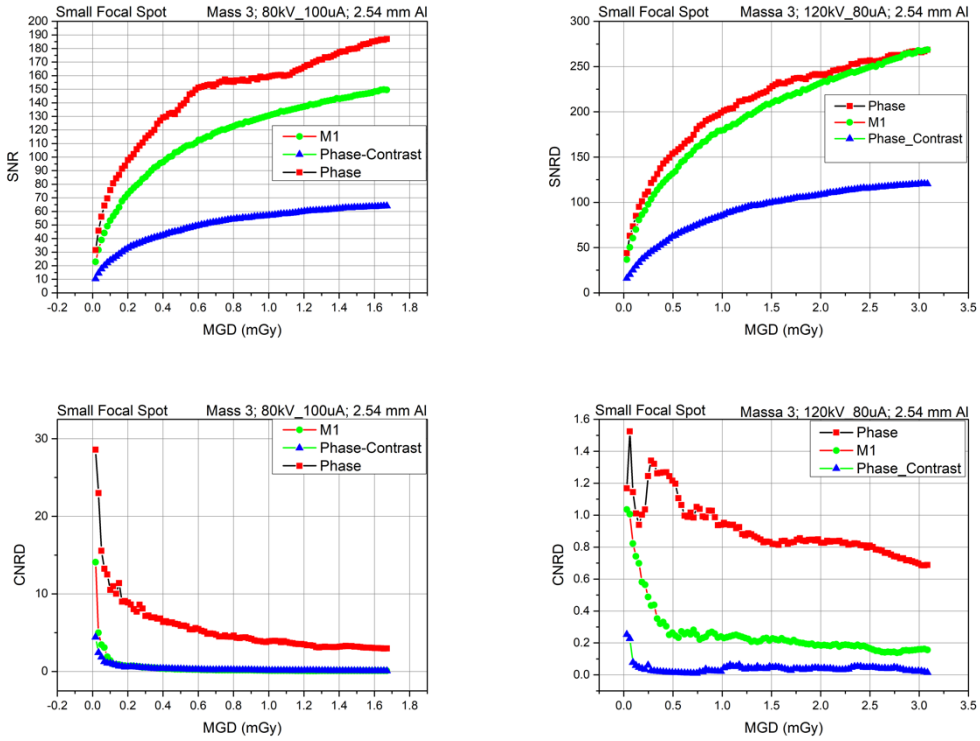

Figure 34: Values of CNR, SNR and CNRD obtained in detecting mass #3, using the small focal spot for two different tube voltages.

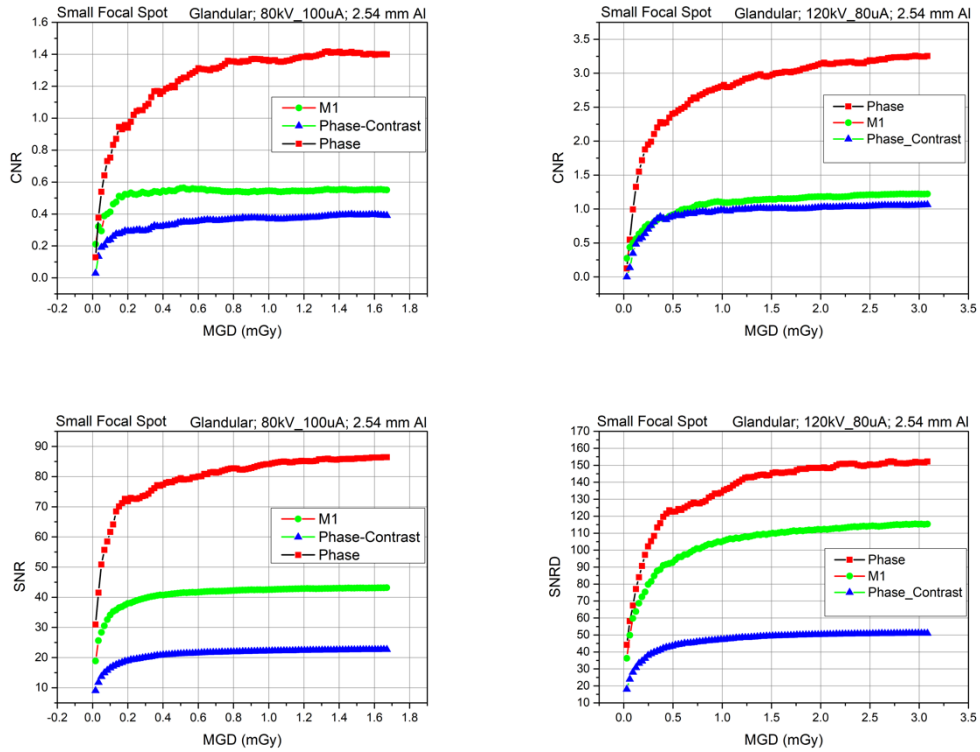

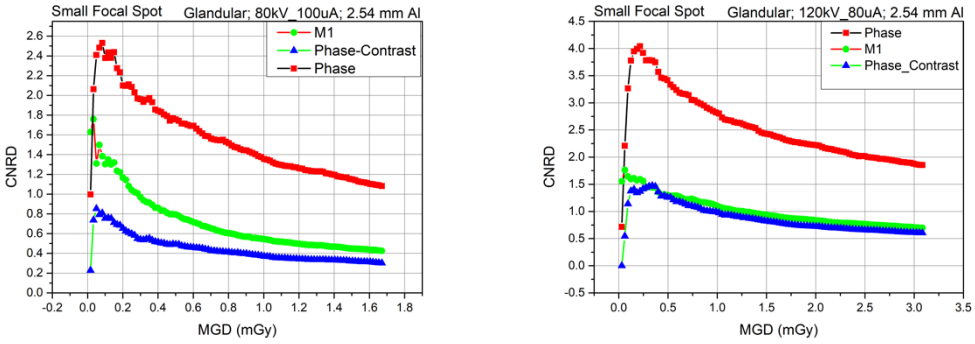

Figure 35: Values of CNR, SNR and CNRD obtained in detecting glandular tissue, using the small focal spot for two different tube voltages.

In figure 32 and 33 it is possible to see that image quality parameters, using the large focal spot, have higher values for absorption-based images than for phase contrast and phase images, due to lower exposure on the detector at any fixed value of MGD. In table 12 are reported the image quality parameters for both glandular tissue and mass #3, using the large focal spot.

In figure 34 and 35 it is possible to see that image quality parameters, using the small focal spot, have higher values for phase images than for phase contrast and absorption, due to the presence of the phase effects that lead to an increase of the image contrast at any fixed value of MGD. In table 13 are reported the image quality parameters for both glandular tissue and mass #3, using the small focal spot.

Tube voltage (kV)	**Imaging method**	**CNR (Sum of 30 images)**	**CNRD (Sum of 30 images)**	**SNR (Sum of 30 images)**	**Large Focal Spot**
80	**Absorption-based**	1.26	0.75	293.5	**Mass 3**
	Phase-contrast	0.41	0.24	152.8	
	Phase	0.58	0.34	81.0	
120	**Absorption-based**	4.00	1.61	482.1	
	Phase-contrast	0.83	0.33	245.5	
	Phase	0.12	0.07	101.6	
	Absorption-based	2.28	1.35	214.7	

80	**Phase-contrast**	1.73	1.02	119.1	**Glandular**
	Phase	1.353	0.80	81.1	
120	**Absorption-based**	3.26	1.31	412.9	
	Phase-contrast	2.49	1.00	200.6	
	Phase	1.38	0.82	103.5	

Table 12: Image quality parameters for both glandular tissue and mass #3, using the large focal spot. The values are reported for a total MGD of 2.845 mGy and 6.176 mGy for 80 kV and 120 kV respectively.

Tube voltage (kV)	**Imaging method**	**CNR (Sum of 100 images)**	**CNRD (Sum of 100 images)**	**SNR (Sum of 100 images)**	**Small Focal Spot**
80	**Absorption-based**	0.14	0.11	149.4	**Mass 3**
	Phase-contrast	0.09	0.07	64.1	
	Phase	3.83	2.96	187.0	
120	**Absorption-based**	0.27	0.56	268.8	
	Phase-contrast	0.03	0.02	120.6	
	Phase	1.21	0.69	268.6	
80	**Absorption-based**	0.55	0.43	43.2	**Glandular**
	Phase-contrast	0.39	0.30	27.7	
	Phase	1.40	1.08	86.4	
120	**Absorption-based**	1.23	0.70	115.3	
	Phase-contrast	1.06	0.61	51.0	
	Phase	3.25	1.85	152.1	

Table 13: Image quality parameters for both glandular tissue and mass 3, using the small focal spot. The values are reported for a total MGD of 1.670 mGy and 3.084 mGy for 80 kV and 120 kV respectively.

2.3.4 Propagation-based phase-contrast and phase retrieval computed tomography

In this third part, we introduce the propagation-based phase contrast computed tomography using the large focal spot and fixing the source-to-object distance ($R_1 = 500\ mm$) and the object-to-image distance ($R_2 = 515\ mm$), with a magnification of $M = 2.03$. The magnification factor with a large distance between object and detector permits sufficient X-ray propagation in order to produce some degree of phase effects in detector space.

A number of 72 projection views, equally spaced over 360°, were acquired and for each view we acquired 5 radiographs (tube current 0.5 mA, exposure time 2.5 s and tube voltage 120 kV and 80 kV).

The values of air KERMA at the isocenter and the total MGD, for a complete rotation around the phantom (sum of 5 images per view) are reported in table 14.

Tube voltage (kV)	**KERMA (mGy) @500 mm**	**MGD (mGy) 1 image**	**MGD (mGy) Complete rotation**
80	0.101	0.095	34
120	0.207	0.206	74

Table 14: Values of air KERMA at the isocenter and total MGD, for a complete rotation around the phantom.

In order to exhibit the phase-contrast of the details embedded in the phantom, we also retrieved the phase map from the phase sensitive projections. In figures 37 and 38 there is a comparison between the reconstruction in phase-contrast and the reconstruction in phase showing the analysis of the microcalcifications embedded in the phantom.

In order to have a quantitative comparison of the two different imaging methods, signal-to-noise ratio (SNR) of the microcalcifications in the phantom was calculated and the values are obtained are reported in table 15.

In all cases analyzed we obtain higher values for phase images than for phase, due to the presence of the phase effects that lead to an increase of the image contrast.

Tube Voltage (kV)	**SNR Phase-Contrast**	**SNR Phase**
80	2.15	3.65
120	1.42	3.80

Table 15: signal-to-noise ratio (SNR) of the microcalcifications in the phantomfor two different tube voltages.

As we can see in figures 37 and 38, the tomographic reconstruction doesn't show the masses embedded in the phantom but only the microcalcifications, in both phase-contrast and phase imaging.

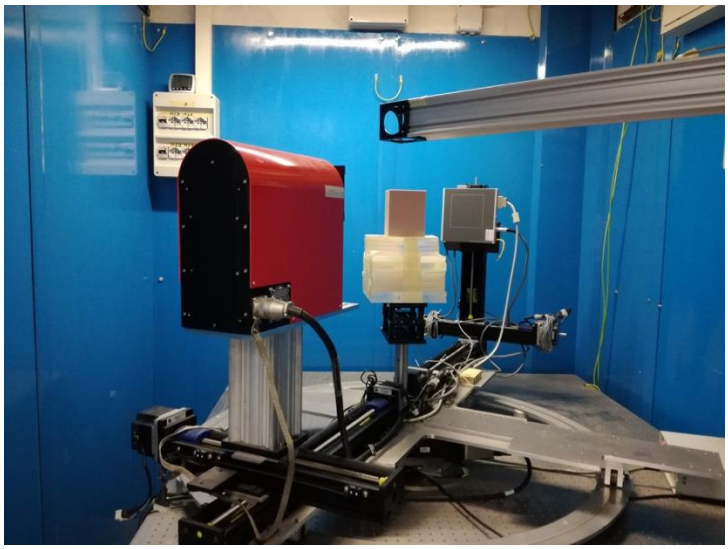

Figure 36: Experimental setup used for tomographic acquisition.

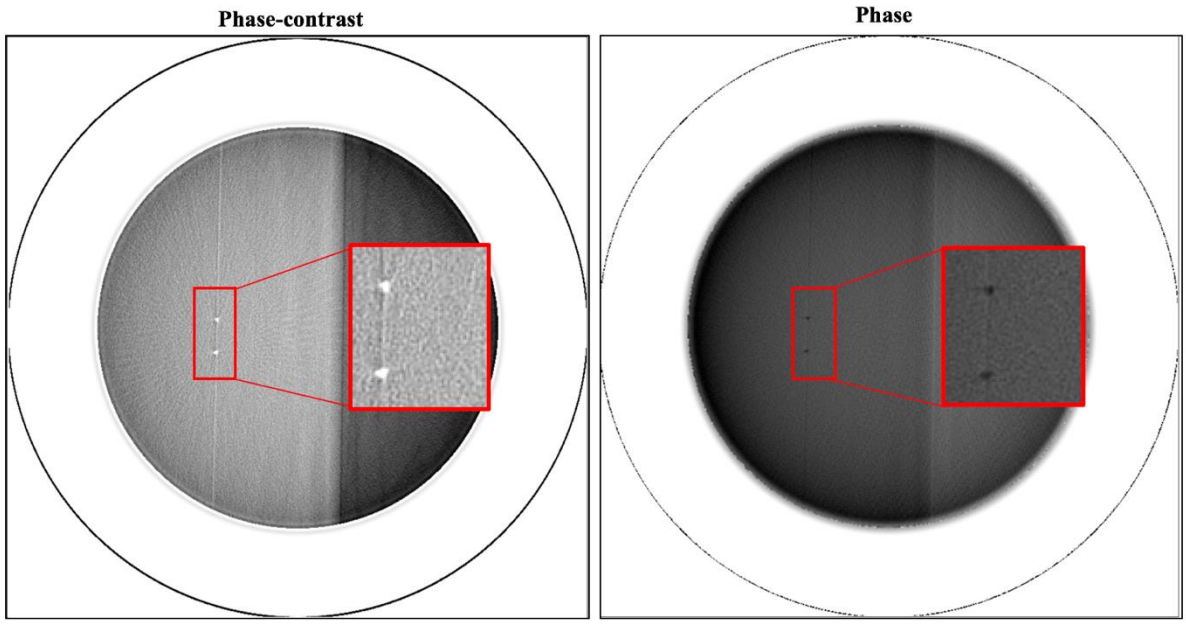

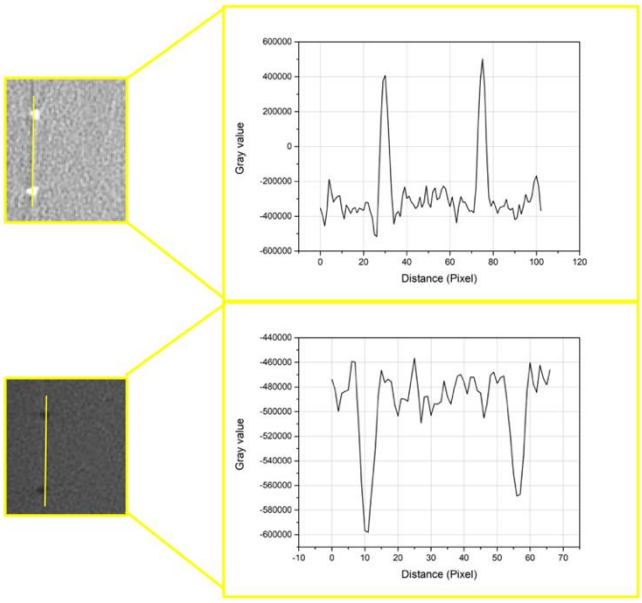

Figure 37: Axial view of a slice acquired in propagation-based phase-contrast computed tomography (sx) and phase computed tomography (dx) of CIRS-014AD phantom (upper part), sum of 5 radiograms for each view (120 kV, 0.5 uA). In the lower part of the image there is the analysis of the microcalcifications (specs in calcium carbonate, 0.39 mm diameter) embedded in the phantom, from a line profile along the specs. The values on the y-axis are inverted from phase-contrast images and phase images because in retrieving the phase map the gray values are inverted.

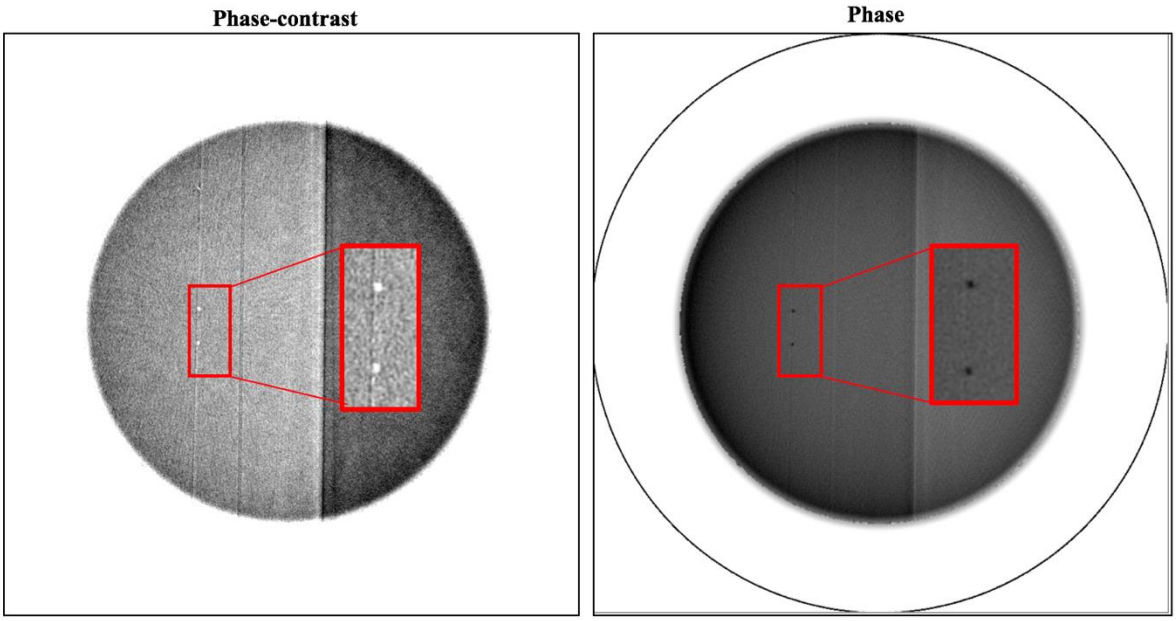

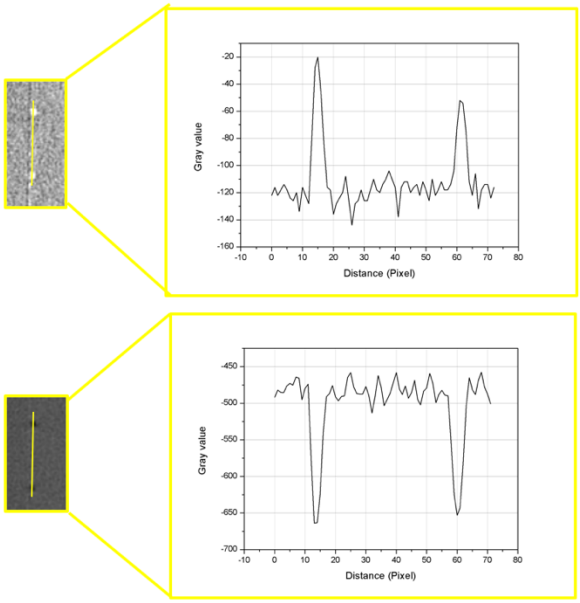

Figure 38: Axial view of a slice acquired in propagation-based phase-contrast computed tomography (sx) and phase computed tomography (dx) of CIRS-014AD phantom (upper part), sum of 5 radiograms for each view (80 kV, 0.5 uA). In the lower part of the image there is the analysis of the microcalcifications (specs in calcium carbonate, 0.39 mm diameter) embedded in the phantom, from a line profile along the specs. As in the previous case, the values on the y-axis are inverted from phase-contrast images and phase images because in retrieving the phase map the gray values are inverted.

2.3.4 Propagation-based phase-contrast and phase retrieval tomosynthesis

In this fourth part of the work, we introduce the propagation-based phase contrast tomosynthesis and the attenuation-based tomosynthesis using the large focal spot and fixing the source-to-object distance ($R_1 = 500\,mm$) and the object-to-image distance ($R_2 = 515\,mm$), with a magnification of $M = 2.03$.

A number of 25 projection views, equally spaced over 50°, were acquired and for each view we acquired 5 radiographs (tube current 0.5 mA, exposure time 2.5 s and tube voltage 120kV). The air KERMA at the isocenter was 0.207 mGy (0.206 mGy of MGD) and the total MGD, for a complete rotation around the phantom (sum of 5 images per view), is 26 mGy.

In order to exhibit the phase-contrast of the details embedded in the phantom, we also retrieved the phase map from the phase sensitive projections. In figure 39 there is a comparison between the reconstruction in absorption-based, phase-contrast and in phase showing the analysis of the microcalcifications embedded in the phantom.

Even in this case, as we can see in figure 39, the tomosynthesis does not show the masses embedded in the phantom but only the microcalcifications.

In order to have a quantitative comparison of the three different imaging methods, signal-to-noise ratio (SNR) of the microcalcifications in the phantom was calculated and the values are obtained are reported in table 16.

In all cases analyzed we obtain higher values for phase images due to the presence of the phase effects that lead to an increase of the image contrast.

Tube Voltage (kV)	SNR Attenuation	SNR Phase-Contrast	SNR Phase
120	3.99	2.55	9.02

Table 16: signal-to-noise ratio (SNR) of the microcalcifications in the phantom for three different imaging method.

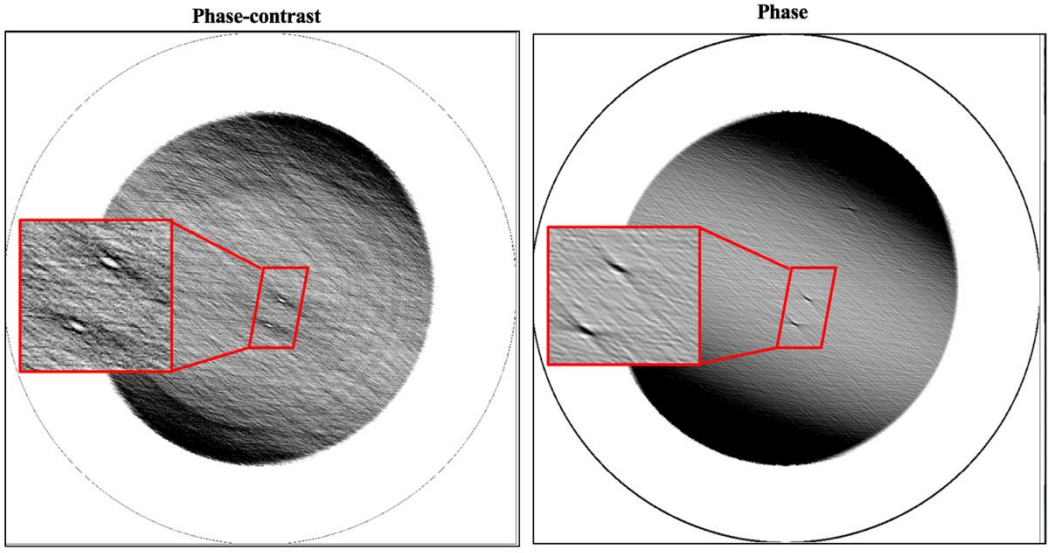

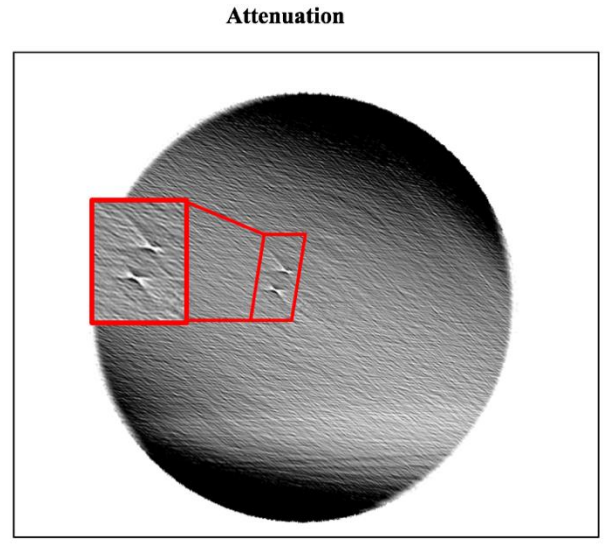

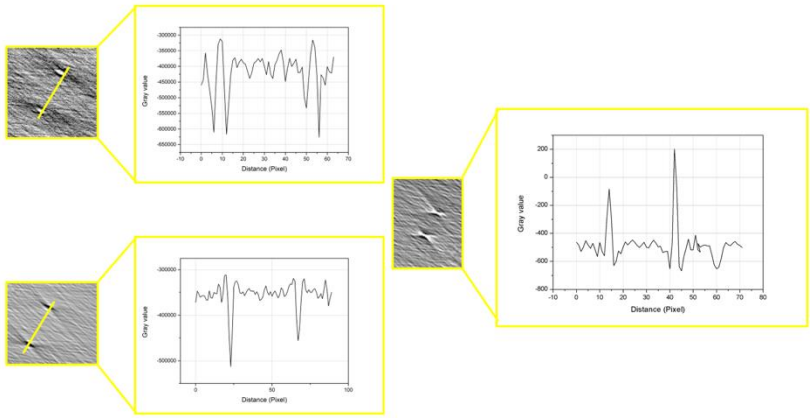

Figure 39: Axial view of a slice acquired in tomosynthesis of CIRS-014AD phantom (upper part) for three different images techniques, sum of 5 radiograms for each view. In the lower part of the image there is the analysis of the microcalcifications (specs in calcium carbonate, 0.39 mm diameter) embedded in the phantom, from a line profile along the specs. Analyzing the profiles, we can notice that the values on the y-axis are inverted from phase-contrast images and phase images because in retrieving the phase map the gray values are inverted. In particular, the images acquired in phase does not show the artefacts seen in phase-contrast images because the Paganin's algorithm used for retrieve the phase map operates as a filter useful to reduce the artefacts.

Conclusions

The aim of this work was to investigate the possible improvement in contrast in phase-contrast high energy imaging with respect to attenuation-based imaging. In particular, we investigated the image quality for detection of simulated micro-calcifications and masses in a breast mammographic phantom (50% glandular/50% adipose).

This study demonstrates the potential benefits of utilizing a high energy X-ray phase sensitive system for breast imaging applications. Due to the limited output power of the micro focus X-ray tube, a high energy X-ray beam is required for phase imaging to reduce the exposure times to clinically acceptable values.

The aim of the research was focused on the use of the phase contrast phenomenon for better visibility of structures such as microcalcifications and tumor masses, in order to improve the quality of the image and to obtain a better diagnosis.

From the projection views of the phantom acquired using the large focal spot it is possible to see that image quality parameters have higher values for absorption-based images than for phase contrast and phase images, due to higher exposure on the detector. However, using the small focal spot, image quality parameters have higher values for phase images due to the presence of the phase effects that lead to an increase of the image contrast.

This result can be explained because for soft tissue ($Z < 11$) and its equivalent materials, attenuation-based imaging using high values of tube voltage lead to an inferior contrast due to their weak attenuation properties. Phase-sensitive imaging, instead, allows to utilize high energy X-rays for imaging soft tissue at low dose levels. In addition to this, a small focal spot is necessary to limit geometric blurring and achieve adequate spatial resolution.

The SNR and CNR improvements provided by the phase-sensitive images was sufficient to detect the smallest masses and microcalcifications.

For example, analyzing the hemispheric mass 3 (3.16 mm thickness) the reported contrast for phase contrast imaging was 0.027 versus 1.208 for the phase imaging, underlying the improvement in contrast resolution. Similarly, for smaller masses of 1.98 mm thickness, the reported contrast for phase contrast imaging was 0.255 versus 0.606 for the phase imaging, confirming the previous result.

Analyzing the images acquired in propagation-based phase-contrast computed tomography, we can only see the presence of the microcalcifications. The masses embedded in the phantom have a hemispheric shape and are made up of 75% glandular tissue, so they aren’t visible in the reconstruction.

Also in tomographic reconstruction we retrieved the phase map of the images acquired and in order to have a quantitative comparison of the two different imaging methods, signal-to-noise ratio (SNR) of the microcalcifications in the phantom was calculated. The values obtained are of 1.42 for propagation-based phase contrast reconstruction and of 3.80 for the phase map reconstruction, so, even in this case, there is an improvement in phase imaging.

For the images acquired in propagation-based phase contrast tomosynthesis, only the microcalcifications are visible and, even in this case, the SNR assumes higher values for phase reconstruction. The values obtained are of 3.99 for absorption-based reconstruction, of 2.55 for the phase contrast reconstruction and of 9.02 for the phase reconstruction.

In conclusion we can say that phase contrast imaging technique demonstrate the edge enhancement effect at the interfaces of different tissues or materials while providing additional CNR for the diagnostic purposes.

X-Ray phase-contrast imaging (PCI) techniques are innovative methods that may overtake the limitations of conventional radiology. The advantage of phase contrast over conventional absorption contrast even grows with increasing energy. Furthermore, because the phase contrast image formation is not intrinsically linked to the absorption of X-rays in the sample, the absorbed dose can potentially be reduced by using higher X-ray energies.

This study demonstrated the potential of high energy phase sensitive x-ray imaging to improve the detection of masses and microcalcifications and reduce radiation dose. Future studies will utilize several phantoms, including those representing more complex anatomical tissue structures of the breast.

References

[1] Associazione Italiana Per la Ricerca sul Cancro (AIRC) https://www.airc.it/tumori/tumore-al-seno.asp#nav8

[2] Rosenberg, Robert D., et al. "Effects of age, breast density, ethnicity, and estrogen replacement therapy on screening mammographic sensitivity and cancer stage at diagnosis: review of 183,134 screening mammograms in Albuquerque, New Mexico." *Radiology* 209.2 (1998): 511-518.

[3] Berg, Wendie A., et al. "Detection of breast cancer with addition of annual screening ultrasound or a single screening MRI to mammography in women with elevated breast cancer risk." *Jama* 307.13 (2012): 1394-1404.

[4] Pelliccia D., Kitchen M. J., Morgan K. S., in: "Handbook of X-ray Imaging: Physics and Technology", cap. 49 (Russo P. Ed.) CRC Press (2018): 971-980.

[5] Suortti P., Keyrilainen J., M. J., Thomlinson W., in: "Handbook of X-ray Imaging: Physics and Technology", cap. 51 (Russo P. Ed.) CRC Press (2018): 1025-1036.

[6] Zysk, Adam M., et al. "Adaptation of a clustered lumpy background model for task-based image quality assessment in x-ray phase-contrast mammography." *Medical physics* 39.2 (2012): 906-911.

[7] Dreossi D., "The mammography project at the SYRMEP beamline", European Journal of Radiology, Volume 68, Issue 3, S58 – S62.

[8] Auweter, S. D., et al. "X-ray phase-contrast imaging of the breast—advances towards clinical implementation." *The British journal of radiology* 87.1034 (2014): 20130606.

[9] Castelli E, Tonutti M, Arfelli F, Longo R, Quaia E, Rigon L, et al. Mammography with synchrotron radiation: first clinical experi- ence with phase-detection technique. Radi- ology 2011; 259: 684–94. doi: 10.1148/ radiol.11100745.

[10] Dreossi D, Abrami A, Arfelli F, Bregant P, Casarin K, Chenda V, et al. The mammog- raphy project at the SYRMEP beamline. Eur J Radiol. 2008; 68(Suppl. 3): S58–62. doi: 10.1016/j.ejrad.2008.04.038.

[11] Pani S, Longo R, Dreossi D, Montanari F, Olivo A, Arfelli F, et al. Breast tomography with synchrotron radiation: preliminary results. Phys Med Biol 2004; 49: 1739–54.

[12] Grandl S, Willner M, Herzen J, Mayr D, Auweter SD, Hipp A, et al. "Evaluation of phase-contrast CT of breast tissue at conventional X-ray sources—presentation of selected findings". Z Med Phys 2013; 23: 212-21. doi: 10.1016/ j.zemedi.2013.02.005.

[13] Paganin, David, et al. "Simultaneous phase and amplitude extraction from a single defocused image of a homogeneous object." *Journal of microscopy* 206.1 (2002): 33-40.

[14] Sarno, Antonio, et al. "Cone-beam micro computed tomography dedicated to the breast." *Medical Engineering and Physics* 38.12 (2016): 1449-1457.

[15] CIRS (Computerized Imaging Reference System Inc.) http://www.cirsinc.com/products/modality/45/mammography-phototimer-consistency-testing-slabs/

[16] Richard Hammerstein, G., et al. "Absorbed radiation dose in mammography." *radiology* 130.2 (1979): 485-491.

[17] Boone, John M. "Glandular breast dose for monoenergetic and high-energy x-ray beams: Monte Carlo assessment." *Radiology*213.1 (1999): 23-37.

[18] https://www.ts-imaging.net/Services/Simple/ICUtilAbsorb.aspx

Acknowledgements

Al termine di questo lavoro di tesi sento di dover ringraziare tutte le persone che mi hanno accompagnata, supportata e “sopportata”.

Un primo grande, grandissimo e sentito ringraziamento va al mio relatore, il professore Russo, che in soli due anni è riuscito a comprendere a fondo chi è la vera Francesca, che mi ha spinto a lavorare sempre più duramente perché solo con il duro lavoro, la passione e la curiosità si possono raggiungere gli obbiettivi più grandi. Ringrazio ancora il professore Russo perché mi ha dato tante opportunità. In fondo i suoi studenti non sono altro che figli acquisiti, grazie.

Voglio ringraziare il professore Mettivier, i cui consigli sono arrivati sempre nei momenti in cui ne avevo disperato bisogno e, anche se lui non lo sa, mi ha aiutato a superare molte difficoltà sperimentali che mi sembravano insormontabili.

Ringrazio ancora il professore Roca, persona paziente e disponibile che mi ha aiutata a rendere questa tesi comprensibile anche a chi è lontano dal campo della fisica medica.

Ringrazio il dott. Antonio Sarno perché mi ha insegnato tanto ed ha avuto pazienza. Senza i suoi preziosi consigli non avrei potuto portare a termine questo lavoro. Vedo in lui un ottimo docente e spero che un giorno possa diventare un mentore per tanti studenti, così come lo è stato per me.

Ringrazio, inoltre, la dottoressa Francesca Di Lillo per esserci stata nei momenti più brutti, diventando un punto di riferimento fondamentale, perché so che se non ci fosse stata lei non avrei potuto concludere questa esperienza.

E in ultimo, ma non per importanza, ringrazio le ragazze del laboratorio. Voglio ringraziarle per i sorrisi, per il supporto, per le risate, per le giornate interminabili e per la condivisione di tutti i momenti, belli e brutti. Siamo diventate un’unica grande famiglia e per quanto i cammini che intraprenderemo saranno diversi, rimarremo sempre unite, perché in fondo le TESISTE non potranno essere dimenticate.